Supplementary Material and Methods for "An increasing Arctic-Boreal CO_2 sink despite strong regional sources"

Anna-Maria Virkkala, Brendan M. Rogers, Jennifer D. Watts, Kyle A. Arndt, Stefano Potter, Isabel Wargowsky, Edward A. G. Schuur, Craig See, Marguerite Mauritz, Julia Boike, Syndonia M. Bret-Harte, Eleanor J. Burke, Arden Burrell, Namyi Chae, Abhishek Chatterjee, Frederic Chevallier, Torben R. Christensen, Roisin Commane, Han Dolman, Bo Elberling, Craig A. Emmerton, Eugenie Euskirchen, Liang Feng, Mathias Goeckede, Achim Grelle, Manuel Helbig, David Holl, Järvi Järveoja, Hideki Kobayashi, Lars Kutzbach, Junjie Liu, Ingrid Liujkx, Efrén López-Blanco, Kyle Lunneberg, Ivan Mammarella, Maija E. Marushchak, Mikhail Mastepanov, Yojiro Matsuura, Trofim Maximov, Lutz Merbold, Gesa Meyer, Mats B. Nilsson, Yosuke Niwa, Walter Oechel, Sang-Jong Park, Frans-Jan W. Parmentier, Matthias Peichl, Wouter Peters, Roman Petrov, William Quinton, Christian Rödenbeck, Torsten Sachs, Christopher Schulze, Oliver Sonnentag, Vincent St.Louis, Eeva-Stiina Tuittila, Masahito Ueyama, Andrej Varlagin, Donatella Zona, and Susan M. Natali

Correspondence: avirkkala@woodwellclimate.org

1. Study domain

Our study covers the Arctic-Boreal zone (ABZ) which was delineated based on the tundra and boreal biomes included in Dinerstein et al. (2017) [1]. The tundra consists of treeless Arctic and sub-Arctic ecosystems, and the boreal biome is dominated by forests. Both of the biomes also include wetlands. In total, 23% of the ABZ is covered by larch forest, 38% by other types of forests (evergreen, mixed, deciduous broadleaved), 6% by wetlands, and 14% by sparse boreal vegetation that is not classified as a forest, 13% as tundra vegetation covered by shrubs, grasses, mosses, and lichens, and 6% as barren tundra with minimal vegetation, based on the land cover dataset used in this study (Supplementary Table 3). 77% of the ABZ contains permafrost which is ground that remains frozen for at least two consecutive years [2]. Our study does not focus on the entire permafrost region that also includes the alpine permafrost regions further south in the Tibetian plateau, Alps, and Rockies mountain chains, for example.

2. In-situ flux data summary

2.1. Data screening and filtering

We used the full Arctic-boreal CO_2 flux (ABCflux) database [3,4] with the following modifications. In instances where chamber plots from the same site had the same coordinates, we calculated an average flux for each year and month across the chamber plots (1-12 plots per site). This was done to assure that these measurements better represent average landscape-scale conditions of the site that could be more easily linked to the geospatial data sets and compared with eddy covariance measurements. We further filled flux columns that remained NA even though the two other flux columns had data by subtracting the two flux values using variations of the equation NEE= GPP-R_{eco}. We only included sites within our Arctic-boreal domain (i.e. tundra and boreal biomes as defined in Dinerstein et al. (2017) [1]), thus a few hemiboreal sites were excluded.

We removed outlier observations showing extremely high July NEE uptake in the tundra with the Study_ID_Short identifier "Lund_Kobbefjord_Ch" with uptake values < -300 g C m^{-2} $month^{-1}$ in Greenland (range of tundra July NEE primarily between -25 to -100 g C m^{-2} $month^{-1}$). Moreover, we removed observations with the Study_ID_Short "Goulden_CA-NS2_tower2", "Goulden_CA-NS3_tower3", "McCaughey_CA-Man" showing high GPP values in the peak winter months (GPP 100-300 g C m^{-2} $month^{-1}$ in January or February compared to the overall December-February range between -20 to 74 g C m^{-2} $month^{-1}$). The final list of sites can be found in Supplementary Table 2.

2.2 Data description

The final data used in 1-km models included 199 sites and 4,981 months in total. The sample sizes for the different fluxes and model resolutions can be found in Supplementary Table 4. The majority of the data for the 1-km models was based on eddy covariance: 55% of sites and 88% of months represented this approach. Each site had from one to 213 months of measurements in our database, with the average number of months per site being 25. Long-term sites with more than 7 years of year-round data included boreal forest sites (FI-Hyy, FI-Sod, CA-Oas, CA-Obs, CA-Gro, US-Uaf, SE-Deg), a wetland site (FI-Kaa), and a tundra site (US-EML). Across all the sites, most of the sites were in recently undisturbed ecosystems (i.e., ecosystems without known abrupt changes related to, e.g., fires, forest harvesting, thermokarst). There were 21 sites that had experienced a fire; two of these had data from recent years (from Alaska). 3 sites reported thermokarst; 2 of these were in Alaska and 1 in Siberia, but gradual permafrost thaw was present in many more sites. At least 5 forest sites had been harvested. In total, 14% of the sites in ABCflux have experienced some level of natural or anthropogenic disturbances. This proportion is likely less than the overall proportion of disturbances across the entire ABZ. For example, 11% of the ABZ was burned during the 2002-2020 period [5], and the areas experiencing thermokarst and harvesting are also extensive. Thus, the flux site distribution might be biased towards non-disturbed or only moderately disturbed sites [6,7], leading to potential underestimations in disturbance effects on CO_2 emissions.

The most represented vegetation types in our database were evergreen needleleaf forests (26% of sites and 41% of months), shrub tundra (15% of sites and 10% of months), and wetlands (11% of sites and 15% of data). Note that these vegetation type statistics were based on the information extracted from the gridded land cover data set and were thus slightly different from those reported in Virkkala et al. (2021).

2.3. A description of the in-situ flux variability

Average net CO_2 uptake during 2001-2020 was highest in July (Supplementary Fig. 7), both in the tundra and boreal, during which time almost all observations (95%) were net sinks. In the tundra, net uptake was high primarily in July while it was high during all the summer months in the boreal: during June and August in the tundra, the rate of carbon uptake was two to three times less compared to boreal ecosystems (Supplementary Fig. 7). Non-summer season (September-May) net emissions were highest in October, both in the tundra (average in-situ NEE 13 ± 12 g C m^{-2} $month^{-1}$) and the boreal regions (average in-situ NEE 17.7 ± 17 g C m^{-2} $month^{-1}$). In both biomes, average non-summer season NEE and R_{eco} were greater than zero in all months (excluding May in the boreal). 8% of the in-situ fluxes also show net uptake in autumn and spring months (Supplementary Fig. 19; excluding May). The magnitude of average monthly CO_2 fluxes was relatively similar in both biomes across the peak winter months (December-February, in-situ NEE ranging from 9 to 14 g C m^{-2} $month^{-1}$ in the boreal and 7 to 8 g C m^{-2} $month^{-1}$ in the tundra). Furthermore, net emissions in the tundra in May and September were even higher than in the boreal.

It is worth noting that while we had up to 10 years of data from three Siberian larch forest sites, the only year-round site was located in an ecotone close to the tundra experiencing permafrost thaw, and was a small annual CO_2 source [8]. The other two larch sites had some of the strongest growing season fluxes that might also indicate strong annual CO_2 sinks (e.g., -240 g C m^{-2} $month^{-1}$ for July compared to ca. -150 g C m^{-2} $month^{-1}$ for the evergreen forests). Furthermore, Siberian tundra sites in relatively similar coastal graminoid-dominated vegetation types had a large variability from relatively strong sinks to large CO_2 sources with average annual NEE ranging from -37 to +60 g C m^{-2} $year^{-1}$.

3. Geospatial data

Predictors included in our models and their main theoretical links to fluxes are listed in Supplementary Table 3.

3.1 Processing geospatial data

To build a continuous dataset of gridded predictor variables, we had to gap-fill some of the predictor data (NDVI) and/or include some lower-level quality data (LST). We gap-filled and smoothed MODIS NDVI at their original temporal resolution using the method developed by Kong et al. (2019) [9]. This denoising method uses weighted Whittaker approach [10] with parameter λ across space for reconstructing gap-filled and smoothed remote sensing vegetation index time series and was efficiently employed in Google Earth Engine (see here https://github.com/gee-hydro/gee_whittaker_kong2019_validation). All the available NDVI data were used but were weighted to account for good and poor quality data (e.g., snow), and the algorithm was run three times to optimize performance. We used the most recent and efficient version of this algorithm with a constant parameter λ found here (https://code.earthengine.google.com/09fef6c8c16919f8ecaa455aae5362b0). The gap-filling and smoothing method with constant λ used here was originally developed for LAI. Therefore, the available scripts developed by Kong et al. (2019) had to be adjusted for NDVI. The λ parameter was manually optimized by comparing the effects of λ set to 10-700.

The GIMMS3g NDVI data includes gap-filled data provided by the data developers (flag 1: NDVI retrieved from spline interpolation, flag 2: NDVI retrieved from seasonal profile, possible snow/cloud). We used the NDVI values with a quality flag 2 if no other information was available (during the winter). During the summer, we used NDVI values with flag 1 to gap-fill data. Small remaining gaps were filled with linear interpolation.

We acknowledge the uncertainties associated with gap-filling NDVI data throughout the snowy shoulder and winter seasons but took this approach to assure that our predictors have data throughout the entire year, as most of the machine learning models cannot deal with missing data accurately. We justified this decision further by the fact that we are using these data to train multivariate models where, for example, climate data is likely the most important predictor instead of the gap-filled (and temporally not variable) optical remotely sensed data during the winter. We further supported this approach with the idea that vegetation biomass (and greenness) generally stays the same (or is lower) after the last good-quality autumn pixel value throughout the winter. We verified that the winter values were higher in highly productive ecosystems (e.g., forests, where winter NDVI values were close to 0.5) compared to sparse ecosystems (e.g., tundra, where winter NDVI values were close to 0-0.2) to make sure that the vegetation indices differ spatially in expected ways. We extracted the final predictor values at our flux sites from this gap-filled and smoothed data. These correlated significantly with the non-gap-filled values in the summer (Pearson correlation 0.88).

The geospatial data had differences in spatial resolution and terrestrial surface coverage (e.g., lake and ocean distribution) and ABCflux site coordinate accuracy was also variable. Therefore, in cases where some sites and/or monthly observations would have received NA values, we extracted the closest non-NA pixel values. This way we were able to keep all the sites from this sparsely measured region in the analysis.

3.2 Additional predictors that were tested

We tested several other data sources as predictors for our models in addition to the ones listed on Supplementary Table 4. Those were dropped because (i) they were highly correlated with the other more powerful predictors that we already had (e.g., MOD13A2v006-based NDVI chosen over EVI or MOD11A2v006 surface temperature over TerraClimate-based air temperature for 1-km models; a Pearson correlation higher than 0.8 was considered as a cutoff value), (ii) they had data from a temporal period that was shorter than our study period (e.g. fractional open water cover 2002-2015 or ESA CCI annual permafrost layers 1998-2017 [11,12]), (iii) they had unrealistic values within our study domain (e.g., pixels indicating frozen status along the Swedish coastline in July [13], or (iv) they were missing a lot of data from the northernmost latitudes (e.g., northern Greenland) or coastlines.

Some potentially important variables were difficult to aggregate to ecologically meaningful predictors to be used in our monthly models. Describing fire history was one of those predictors as no accurate circumpolar burn history products exist that would extend beyond our study period that would allow us to accurately describe how, for example, a site/pixel that burned in 1970 is recovering after the fire. We tested including a ‘time since fire’ predictor based on MCD64A1v006 that goes up to 2020 [14] or GFED4 that goes up to 1997 [15] for each monthly observation to our machine learning model, but this variable was among the least important variables for all fluxes during the test runs (results not shown), likely due to its limitations in long-term data coverage. Additional predictors that were tested but excluded due to low importance included thermokarst coverage [16] and forest age in 2010 [17].

4. Machine learning models

4.1 Model structure

We had three response variables (GPP, R_{eco}, and NEE) and two different spatial resolutions and time periods of models. Consequently, we built a total of six models. We used the same predictors for all the response variables and a similar set of predictors for the 1-km and 8-km models to allow for straightforward model and prediction comparisons. For example, we used MODIS tree cover for the 1-km model and AVHRR tree cover for the 8-km model, and MODIS LST for the 1-km model and TerraClimate air temperature for the 8-km model.

We used random forest models which are a powerful machine learning model. They utilize several decision trees in an ensemble model framework and thus avoid overfitting, have high accuracy, are highly adaptable, and are not significantly impacted by outliers. Random forest models bootstrap the data several times and sample the predictor variables at each split during the tree building, after which the algorithm builds an ensemble prediction [18] . However, random forest models may suffer from overfitting and extrapolating outside the conditions present in the training data [19]. We tested other machine learning models (e.g., support vector machine, generalized boosted regression tree, generalized additive model, neural networks; results not shown). Random forest models outperformed those in terms of cross-validated predictive performance and produced the most realistic flux maps, which is why we only used random forest models.

For all the random forest models, we assumed Gaussian error distribution. Parameters for machine learning models were tuned separately for each response variable with the "caret" package in R [20,21] using the leave-one-site-out cross validation. We tuned the number of variables randomly sampled as candidates at each split from three options in each model. The best model with the final set of parameters was chosen based on the lowest root mean square error (RMSE) values. The only parameter that was tuned was the number of variables to randomly sample as candidates at each split, and it varied from 2 to 17 in the final models depending on the response variable.

We used partial dependence plots (i.e., response graphs) using the "pdp" package [22] and estimated variable importance of the predictors from each of the models using the "vip" package [23] (Section Machine learning models in the main text).The values on the y axis of each partial dependence plot can be interpreted as followed: yhat is conditional on other predictors in the model and their relationships with the predictor in the plot in question. Therefore, yhat values should not be directly compared with observed or predicted values, rather the patterns in yhat should be explored more generally. The x-axis represents the actual predictor values and can be used to infer, for example, conditions that lead to changes in yhat (tipping points), and the strength and direction of the relationship. Variable importance scores were estimated by randomly permuting the values of the predictor in the training data and exploring how this influenced model performance based on RMSE values, with the idea that random permutation would decrease model performance [18]. We used 100 simulations to calculate 100 importance scores which are shown in Supplementary Fig. 5-7.

4.2 Model predictions

We used the random forest models to predict (i.e., upscale) fluxes with the 1-km model from 2001 to 2020 and 8-km model from 1990 to 2016. In total we produced 1692 upscaled flux maps. 8-km upscaled maps were further multiplied by the terrestrial surface cover within each 8-km pixel based on the 1-km ESA CCI+CAVM land cover dataset to remove fluxes from water bodies. These flux maps were robust across the two pixel resolutions, and a comparison of 2001-2016 average annual NEE maps showed that NEE was similar across the two pixel resolutions (Supplementary Fig. 20). The 1- and 8-km predictions had the largest differences in

Siberia, as shown by the annual budget mismatches in Fig. 4, which also prevented us from merging the two predictions and calculating trends for the entire 1990-2020 period. We also compared upscaled NEE maps from two approaches: based on modeling NEE directly, and deriving it indirectly from the upscaled GPP and R_{eco} maps. NEE from these two approaches yielded similar results, providing confidence in our results. Budgets estimates from the NEE and GPP-R_{eco} approaches are also similar (Table 1, Supplementary Table 1, Supplementary Fig. 20, Supplementary Fig. 21-22). Overall, our upscaling results revealed a latitudinal pattern of average CO_2 fluxes, with stronger sinks in the south and weaker sinks or sources in the north (Fig. 1). However, the correlation between latitude and average NEE was moderate (Pearson's correlation for in-situ NEE: 0.26, p=0.053; for upscaled NEE: 0.55, p<0.001), suggesting that the latitudinal climate and radiation gradients were not the sole drivers of spatial CO_2 flux patterns.

4.3 Model predictive performance and uncertainty

The predictive performance and uncertainty analysis was described in detail in the Machine learning modeling section of the Online methods. Here we provide a longer description of the strengths and limitations of our random forest models.

Overall, our models show good predictive performance. Compared to earlier ABZ upscaling efforts, our cross-validated performance metrics (Supplementary Figs. 1-3) indicate better performance. For example, the R^2 of our models ranged from 0.5 to 0.78, whereas Natali et al. (2019) [24] had an R^2 of 0.49 for winter NEE and Virkkala et al. (2021) [3] an R^2 of 0.07 for annual NEE, R^2 of 0.5 for annual GPP and annual R_{eco}; note though that the cross validation in Natali et al. 2019 was not based on a leave-one-site out approach. However, our performance metrics also indicate that strong sinks and sources, and high GPP and R_{eco} were underestimated - a common issue in any kind of modeling (Tramontana et al. 2016). As described with the mean bias error (MBE) metric, the models had a small tendency to underestimate fluxes (i.e., NEE models were predicting larger net uptake than net emissions), as reflected by the small and positive MBE values. However, the majority of the observed and predicted values were close to the 1:1 line, and issues associated with the model underestimating strong net sinks were clearly larger (deviation up to -150 g C m^{-2} $month^{-1}$) than the model underestimating strong net sources (deviation up to 80 g C m^{-2} $month^{-1}$). For NEE, it was clear that situations where the modeled month differed significantly from the average monthly flux at the site were predicted worst (shown with yellow and light green values or dark blue values; Supplementary Figs. 1-3). It is thus possible that we are missing predictors that accurately describe conditions from such different months.

We also evaluated how differences in flux measurement method and the exclusion of disturbed sites impact model predictive performance (Supplementary Table 5). Overall, performance statistics were similar across the approaches.

We evaluated the uncertainty of predictions by creating 20 bootstrapped datasets (with replacement; same sample size as in the original model training data) and using those to develop 20 individual models and predictions. For these bootstrapped datasets and models, we did not include the categorical month and land cover datasets as predictors due to bootstrapping resulting in situations where a factor level was entirely missing from the model training data (e.g., for barren class that had little data) which prevented us from predicting fluxes across the entire domain (i.e., predictions to barren class not possible when the model had no information about it). Out of the 20 predictions, we calculated the standard deviation to represent prediction uncertainty. Similar to the predictive performance metrics (largest issues in our models related to predicting strong sinks), the uncertainty analysis also points towards highest uncertainties in areas with strong sinks, such as in northern Europe and southwestern Russia. However, when the uncertainty estimates were presented relative to the average flux, uncertainties were highest in tundra regions and parts of northern boreal Canada which generally have low in-situ flux data coverage. In some areas of these regions, our upscaling shows unrealistically high NEE values. For example, some sparsely vegetated or barren mountainous regions in northern Siberia (Kolyma mountains) or northern Europe (Scandes mountains) showed net emissions of 30-50 g C m^{-2} yr^{-1}, which appears unrealistically high compared to the low vegetation carbon inputs and overall soil carbon pools. However, we did not mask the sparsely vegetated or barren areas away from our upscaling because we had data from these vegetation classes indicating that there is small but significant growing season and annual uptake in these regions [25,26]. Overall, the spatial uncertainty maps thus emphasize uncertainties both associated with model performance with strong sinks, and data gaps.

To further understand the uncertainties related to data gaps, we used a multivariate environmental dissimilarity surface analysis (MESS) to define the area of extrapolation in our models [27]. We used average annual environmental conditions over 2001-2020 of the 7 most important variables for this analysis (solar radiation, NDVI, land surface temperature, soil temperature, snow cover, soil organic carbon stock, soil pH, permafrost probability); average NDVI conditions were calculated for the June-August period alone. MESS represents how similar a point (i.e., a site) is to a reference set of points (i.e., all the ABZ conditions), with respect to a set of predictor variables. Negative values represent sites where at least one variable has a value that is outside the range of environments over the reference set (i.e., areas where the model extrapolates). The values in MESS are influenced by the full distribution of the reference points, so that points within the environmental range of the reference points but in relatively unusual environments will have a smaller value than those in common environments. Large positive values represent common conditions across the sites and ABZ. The analysis was done for the sites with data from January (primarily year-round sites). Our results show that 35% of the region was extrapolated (Supplementary Figure 4). If we limit our budget estimates to the area that was not extrapolated (i.e., 65% of the region), the annual NEE budget was -390 Tg C yr^{-1}.

Despite these uncertainties, our results show that machine learning-based upscaling is a promising approach for understanding recent trends in CO_2 fluxes as the models can easily integrate the most recent flux data and new predictor datasets while operating at high spatial and temporal resolutions. One uncertainty in upscaling remains how natural (e.g., thermokarst, insect outbreaks) and anthropogenic (e.g., forest management) disturbances are covered by the flux sites and explained with gridded data [28]. New predictors describing disturbances as well as supporting and extending the year-round flux network are critical to improve this upscaling and other synthesis and modeling efforts.

5. Comparison with CMIP6 process models, inversions and earlier upscaling efforts

Supplementary Table 6 lists the CMIP6 process models and inversions included in our model intercomparison. The models had variable inputs and structures, which causes differences in model outputs. We used an ensemble of these models (i.e. mean model output) for the two model categories (process and inversion models) because the uncertainty of the ensemble is expected to be lower than the uncertainty of a single model.

The average inversion NEE budget for the entire ABZ, including aquatic ecosystems while excluding fires, indicated a considerably stronger sink strength (-1054 Tg C yr^{-1}; range of individual inversion estimates -259 to -1872 Tg C yr^{-1}). Overall, inversions had a rather high spread of CO_2 fluxes (Supplementary Fig. 17). Spread in inversion budget estimates and pixel-wise fluxes was high across the entire ABZ, demonstrating some level of inversion model disagreement in all parts of the ABZ. The ensemble mean of CMIP6 process models [29] showed consistently stronger tundra CO_2 sink strength (-48 Tg C yr^{-1}) than found in this study and weaker sink strength in the boreal zone (-391 Tg C yr^{-1}) despite the mean NEE budget being very close to ours (-501 Tg C yr^{-1}) (Fig. 1).

We observed high agreement with our upscaling compared to inversion models. However, some disagreements were also apparent, especially in some parts of central and northern Siberia, where our upscaling suggested the region to be primarily a net annual CO_2 source and the inversion ensemble a CO_2 sink; however, the sparsity of year-round atmospheric or terrestrial flux data from this region prevents us from reliably concluding what the current sink status of the region is. Similarly, our upscaling showed sub-Arctic Canada in the Northwest Territories to have a large distribution of annual CO_2 sources whereas inversions suggested sinks. Overall, our combined NEE+fire estimates were on the higher end compared to inversions (i.e. weaker net CO_2 sinks or stronger net CO_2 emissions), especially in Canadian boreal, Siberian boreal, and Siberian tundra regions (Supplementary Fig. 17).

There are some similarities and differences in the long-term trends in our upscaling compared to inversions. Interannual variability in upscaled NEE and inversion-based NEE is highest in Siberia. However, inversions had more interannual variability in flux budgets overall compared to our upscaling. For example, NEE + fire budgets varied by 350 Tg C yr^{-1} in our upscaling whereas those could range by 750 Tg C yr^{-1} in inversion estimates. In our NEE upscaling, interannual variability in NEE was strongly related to air temperature. For example, in 2020 with a record-warm year in Siberia, the NEE budget changed from ca. -400 to -500 Tg C yr^{-1} in Siberian boreal. It is possible that in 2020 Siberian ecosystems also experienced drought that should have decreased uptake as indicated by some of the inversions (Supplementary Fig. 17), which our models did not capture. However, during an extreme disturbance year in 2003 in Siberia with a high extent of fires and a decline in NDVI [30], our upscaling shows an increase in net CO_2 emissions with NEE changing from ca. -300 to -200 Tg C yr^{-1} in the boreal biome and 25 to 40 Tg C yr^{-1} in the tundra biome; this increase of net emissions was shown for most inversions in the Siberian boreal region as well. This provides confidence that our upscaling captures the impact of some of the extreme years that are increasingly important for ABZ CO_2 budgets. A visualization of the pixel-wise fluxes in two extreme years: the 2003 fire year and 2020 warm year are shown in Supplementary Fig. 23.

We also compared our results with the global upscaling product FLUXCOM (RS+METEO NEE ensemble) [28,31,32] that showed a much higher sink strength for the ABZ (tundra budget: -229 Tg C yr^{-1} for 1990-2013 and -225 Tg C yr^{-1} for 2001-2013, boreal budget –964 Tg C yr^{-1} for 1990-2013 and -949 Tg C yr^{-1} for 2001-2013), likely due to ABCfluxv1 including a much more representative set of sites compared to the FLUXNET2015 database [33] used in FLUXCOM (e.g., 136 Arctic sites in ABCflux compared to 5 sites included in FLUXCOM). The higher representativeness comes from our study including also chamber and diffusion through snow measurements, and eddy covariance data that are not found in the global FLUXNET2015 repository. For example, for eddy covariance the ABCflux database includes 2775 monthly fluxes extracted from repositories (FLUXNET2015 and Euroflux and Ameriflux, for example) and 2160 monthly fluxes contributed by site PIs or extracted from publications.

6. Aggregating results

We calculated in-situ cumulative average fluxes by first calculating mean fluxes across years at each site to avoid biasing the statistics by long-term sites. Annual fluxes were calculated for sites that had the full year of monthly flux estimates. We used the package “terra” [34] to derive zonal statistics (mean fluxes and budgets) across the key regions.

Supplementary Tables and Figures

Supplementary Table 1. Average gross primary productivity (GPP), ecosystem respiration (R_{eco}), and net ecosystem exchange (NEE) fluxes and budgets over 2001-2020 across vegetation types. Uncertainties represent standard deviations across sites (for the in-situ data), or across bootstrapped upscaled estimates. Positive numbers for NEE indicate net CO_2 loss to the atmosphere and negative numbers indicate net CO_2 uptake by the ecosystem. Mismatches in the site-level versus upscaled CO_2 fluxes are likely related to sites being biased to certain regions and years while upscaled summaries should provide more representative regional estimates but are influenced by model performance. NAs occurred in situations when flux data was entirely non-existent, not partitioned to GPP and R_{eco}, or when statistics were based on a single site (not possible to calculate standard deviation).

Class	In-situ average NEE g C m^{-2} yr^{-1}	In-situ average GPP g C m^{-2} yr^{-1}	In-situ average R_{eco} g C m^{-2} yr^{-1}	Upscaled average NEE g C m^{-2} yr^{-1}	Upscaled average GPP g C m^{-2} yr^{-1}	Upscaled average R_{eco} g C m^{-2} yr^{-1}	Average NEE budget Tg C yr^{-1}	Average GPP budget Tg C yr^{-1}	Average R_{eco} budget Tg C yr^{-1}
Barren and prostrate shrub	-74 (± 61)	NA	NA	-4 (± 8)	537 (± 23)	513 (± 17)	-4 (± 17)	482 (± 18)	461 (± 15)
Graminoid	10 (± 28)	272 (± 4)	269 (± 0)	9 (± 9)	519 (± 31)	525 (± 23)	6 (± 9)	346 (± 9)	350 (± 6)
Shrub	35 (± 37)	244 (± 44)	288 (± 81)	23 (± 9)	572 (± 35)	598 (± 28)	9 (± 6)	215 (± 5)	225 (± 2)
Sparse boreal vegetation	-33 (± 124)	443 (± 229)	442 (± 135)	35 (± 6)	669 (± 29)	698 (± 27)	50 (± 24)	962 (± 20)	1003 (± 12)
Tree cover, broadleaved, deciduous	-112 (± NA)	1100 (± NA)	988 (± NA)	-185 (± 23)	1568 (± 64)	1433 (± 47)	-90 (± 10)	765 (± 11)	699 (± 10)
Tree cover, needleleaved, deciduous	-17 (± 29)	NA	NA	-61 (± 18)	931 (± 67)	875 (± 52)	-148 (± 45)	2239 (± 32)	2105 (± 26)

Tree cover, needleleaved, evergreen	-36 (± 81)	773 (± 423)	734 (± 431)	-85 (± 12)	1270 (± 47)	1211 (± 34)	-222 (± 37)	3309 (± 48)	3153 (± 29)
Wetland	-22 (± 31)	281 (± 78)	256 (± 67)	-78 (± 11)	778 (± 39)	697 (± 28)	-47 (± 10)	464 (± 9)	415 (± 6)
Mosaic and mixed vegetation	-54 (± 74)	697 (± 265)	643 (± 223)	-117 (± 15)	1358 (± 53)	1274 (± 38)	-102 (± 14)	1188 (± 16)	1114 (± 12)
Alaskan boreal	-7 (± 60)	592 (± 195)	615 (± 148)	-12 (± 10)	495 (± 41)	486 (± 32)	-6 (± 4)	228 (± 4)	224 (± 3)
Alaskan tundra	20 (± 31)	277 (± 90)	298 (± 113)	5 (± 10)	354 (± 28)	360 (± 20)	4 (± 7)	270 (± 6)	274 (± 3)
Canadian boreal	-39 (± 72)	635 (± 255)	598 (± 202)	-32 (± 6)	557 (± 27)	534 (± 20)	-129 (± 26)	2214 (± 31)	2125 (± 22)
Canadian tundra	NA	NA	NA	1 (± 4)	282 (± 13)	278 (± 10)	3 (± 20)	644 (± 20)	636 (± 16)
European boreal	-53 (± 94)	837 (± 583)	778 (± 614)	-64 (± 11)	737 (± 40)	684 (± 30)	-140 (± 20)	1603 (± 23)	1488 (± 16)
European tundra	-42 (± 52)	440 (± 215)	421 (± 232)	14 (± 4)	313 (± 15)	328 (± 12)	10 (± 5)	225 (± 6)	236 (± 4)
Siberian boreal	-105 (± 154)	703 (± NA)	572 (± NA)	-44 (± 9)	535 (± 32)	497 (± 23)	-319 (± 61)	3875 (± 55)	3599 (± 40)

Siberian tundra	-9 (± 30)	241 (± 66)	245 (± 92)	9 (± 5)	296 (± 18)	307 (± 14)	28 (± 24)	910 (± 20)	944 (± 12)

Supplementary Table 2. The sites included in the analysis. For information about the sites see the Virkkala et al. (2021) [4] dataset.

Study ID Short	**Site name**	**Site reference**	**Latitude**	**Longitude**	**Country**	**Flux method**
Adkinson_CA-WP2_tower1	Alberta - Western Peatland - Poor Fen (Sphagnum moss)	CA-WP2	55.5375	-112.334	Canada	Eddy covariance
Adkinson_CA-WP3_tower2	Alberta - Western Peatland - Rich Fen (Carex)	CA-WP3	54.47	-113.32	Canada	Eddy covariance
Alekseychik_RU-Murk_tower1	Mukhrino field station	RU-Murk	60.9	68.7	Russia	Eddy covariance
Aurela_FI-Kaa_tower1	Kaamanen	FI-Kaa	69.14057	27.26985	Finland	Eddy covariance
Aurela_FI-Ken_tower2	Kenttarova	FI-Ken	67.98723	24.24305	Finland	Eddy covariance
Aurela_FI-SamFell_tower3	Sammaltunturi fell	FI-SamFell	67.9733	24.11565	Finland	Eddy covariance
Aurela_FI-Sod_tower1	Sodankyla	FI-Sod	67.36239	26.63859	Finland	Eddy covariance
Aurela_RU-Tks_tower1	Tiksi	RU-Tks	71.59427	128.8878	Russia	Eddy covariance
Backstrand_StordalenMire_Ch	Stordalen Mire	Palsa Site,Sphagnum Site,Eriophorum Site	68.36667	19.05	Sweden	Chamber
BangYong_US-KOC_tower1	US-KOC, Council	US-KOC, Council	64.8439	-163.711	USA	Eddy covariance
Bergeron_CA-sOBS_tower1	Southern Old Black Spruce	CA-sOBS	53.99	-105.12	Canada	Eddy covariance
Bjoerkman_Adventdalen_Diff	Adventdalen, Svalbard	heath shallow,meadow shallow	78.167	16.067	Norway	Diffusion through snow

Bjoerkman_Latnjajaure_Diff	Latnjajaure	heath snowbed,meadow snowbed,heath meadow,mesic meadow, heath shallow	68.333	18.5	Sweden	Diffusion through snow
Boike_NO-Blv_tower1	Bayelva, Spitsbergen	NO-Blv	78.9216	11.8311	Norway	Eddy covariance
Bret-Harte_US-ICs_tower1	Imnavait Creek Watershed	US-ICs	68.6058	-149.311	USA	Eddy covariance
Bret-Harte_US-ICt_tower2	Imnavait Creek Watershed	US-ICt	68.6063	-149.304	USA	Eddy covariance
Cannone_Adventdalen1_Ch	Adventdalen	P1	78.18506	15.92633	Norway	Chamber
Cannone_Adventdalen2_Ch	Adventdalen	P2	78.18511	15.92577	Norway	Chamber
Cannone_Adventdalen3_Ch	Adventdalen	P3	78.18517	15.92551	Norway	Chamber
Cannone_Adventdalen4_Ch	Adventdalen	P4	78.18529	15.92486	Norway	Chamber
Cannone_Adventdalen5_Ch	Adventdalen	P5	78.18534	15.92644	Norway	Chamber
Cannone_Adventdalen6_Ch	Adventdalen	P6	78.18539	15.92581	Norway	Chamber
Cannone_Adventdalen7_Ch	Adventdalen	P7	78.18541	15.92515	Norway	Chamber
Celis_EML_Ch	Eight Mile Lake	moist acidic tundra	63.88306	-149.226	USA	Chamber
Chae_US-KOC_Ch	Council	US-KOC	64.8439	-163.711	USA	Chamber
Christensen_NO-Adv_tower1	Adventdalen	NO-Adv	78.186	15.923	Norway	Eddy covariance
Christiansen_DaringLake_Ch	Daring Lake	Low birch hummock	64.833	-111.633	Canada	Chamber
Christiansen_DiskoIsland_Ch	Disko Island	Arctic Station	69.254	-53.514	Greenland	Chamber
Christiansen_Zackenberg1_Ch	Zackenberg	dry heath	74.467	-20.577	Greenland	Chamber
Christiansen_Zackenberg2_Ch	Zackenberg	Cassiope heath; NY-ITEX heath	74.475	-20.543	Greenland	Chamber
Christiansen_Zackenberg3_Ch	Zackenberg	Salix heath; NY-ITEX heath	74.475	-20.54	Greenland	Chamber
Davydov_Cherskiy1_Ch	Cherskiy	Larch-shrub forest, low density	68.7	161.55	Russia	Chamber
Davydov_Cherskiy2_Ch	Cherskiy	Post-fire shrub	68.72	161.53	Russia	Chamber
Davydov_Cherskiy3_Ch	Cherskiy	Old larch forest	68.73	161.4	Russia	Chamber

Davydov_Cherskiy4_Ch	Cherskiy	Dense larch 'bamboo' stand	68.75	161.45	Russia	Chamber
Dolman_RU-Cok_tower1	Chokurdakh	RU-Cok	70.82914	147.4943	Russia	Eddy covariance
Dolman_RU-Ypn_tower1	Yakutsk	Larix cajanderii stand 160 yr old	62.255	129.619	Russia	Eddy covariance
Dyukarev_Siberia_Ch	Middle Taiga Zone	large hollow,small ridge	60.9	68.7	Russia	Chamber
Eckhardt_LRD_Ch	Lena River Delta	Wet tundra - polygon center,Dry tundra - polygon rim	72.36667	126.4667	Russia	Chamber
Egan/Risk_ImnavaitCreek_Ch	Imnavait Creek	heath	68.607	-149.296	USA	Chamber
Elberling_Endalen_Ch	Endalen, Svalbard	Moist Cassiope heath,Dry Dryas heath,Salix snow bed	78.2	15.6	Norway	Chamber
Elberling_GL-Dsk_tower1	Disko Island	GL-Dsk	69.253	-53.514	Greenland	Eddy covariance
Emmerton_CA-LHazen1_tower1	Lake Hazen, Ellesmere Island	CA-LHazen1	82.82255	-71.3809	Canada	Eddy covariance
Emmerton_CA-LHazen2_tower2	Lake Hazen, Ellesmere Island	CA-LHazen2	81.83447	-71.3846	Canada	Eddy covariance
Euskirchen_RU-Eusk_cher1_tower1	Chersky Tower 1	RU-Eusk_cher1	68.51351	161.5312	Russia	Eddy covariance
Euskirchen_RU-Eusk_cher2_tower2	Chersky Tower 2	RU-Eusk_cher2	68.69808	161.5388	Russia	Eddy covariance
Euskirchen_US-TFBog_tower2	Bonanza Creek Thermokarst Bog	US-BZB	64.69555	-148.321	USA	Eddy covariance
Euskirchen_US-TFBS_tower1	Bonanza Creek Rich Fen	US-BZF	64.69635	-148.324	USA	Eddy covariance
Euskirchen_US-TFRF_tower3	Bonanza Creek Rich Fen	US-BZF	64.70373	-148.313	USA	Eddy covariance
Falk_Zackenberg_Ch	Zackenberg		74.5	-20.5	Greenland	Chamber
Friborg_Se-St1_tower1	Stordalen grassland	Se-St1	68.35415	19.05033	Sweden	Eddy covariance
Friborg_Seida_tower1	Seida	Mixed tundra with upland tundra heath, peat plateau and wetlands	67.05	62.93333	Russia	Eddy covariance
Friborg_Svalbard_Ch	Svalbard	Björnedalen	78.224	15.324	Norway	Chamber
Gasovic_FI-Salm_tower1	Salmisuo	FI-Salm	62.7833	30.9333	Finland	Eddy covariance
Goeckede_RU-Ch2_tower2	Cherski reference	RU-Ch2	68.61689	161.3509	Russia	Eddy covariance

Goulden_CA-NS1_tower1	UCI-1850 burn site	CA-NS1	55.87917	-98.4839	Canada	Eddy covariance
Goulden_CA-NS2_tower2	UCI-1930 burn site	CA-NS2	55.90583	-98.5247	Canada	Eddy covariance
Goulden_CA-NS3_tower3	UCI-1964 burn site	CA-NS3	55.91167	-98.3822	Canada	Eddy covariance
Goulden_CA-NS4_tower4	UCI-1964 burn site wet	CA-NS4	55.91437	-98.3806	Canada	Eddy covariance
Goulden_CA-NS5_tower5	UCI-1981 burn site	CA-NS5	55.86306	-98.485	Canada	Eddy covariance
Goulden_CA-NS6_tower6	UCI-1989 burn site	CA-NS6	55.91667	-98.9644	Canada	Eddy covariance
Goulden_CA-NS7_tower7	UCI-1998 burn site	CA-NS7	56.63583	-99.9483	Canada	Eddy covariance
Goulden_CA-Oas_tower1	Saskatchewan - Western Boreal, Mature Aspen	CA-Oas	53.62889	-106.198	Canada	Eddy covariance
Harazano_US-Cms_tower1	Central Marsh	US-Cms	71.32019	-156.622	USA	Eddy covariance
Helbig_CA-SCB_tower1	Scotty Creek Bog	CA-SCB	61.3089	-121.298	Canada	Eddy covariance
Helbig_CA-SCC_tower1	Scotty Creek Landscape	CA-SCC	61.3079	-121.299	Canada	Eddy covariance
Huemmrich_Utqia?vik_Ch	Utqia?vik	wet sedge tundra	71.322	-156.602	USA	Chamber
Humphreys_CA-CB_tower1	Cape Bounty	CA-CB	74.915	-109.574	Canada	Eddy covariance
Iwata_US-Rpf_tower1	Poker Flat Research Range: Succession from fire scar to deciduous forest	US-Rpf	65.11983	-147.512	USA	Eddy covariance
Iwata_US-Uaf_tower1	University of Alaska, Fairbanks	US-Uaf	64.86627	-147.856	USA	Eddy covariance
Jarveoja_DegeroStormyr_Ch	Degerö Stormyr	oligotrophic minerogenic mire complex	64.18333	19.55	Sweden	Chamber
Kade_ImnavaitCreek1_Ch	Imnavait Creek	wet sedge	68.606	-149.311	USA	Chamber
Kade_ImnavaitCreek2_Ch	Imnavait Creek	tussock	68.606	-149.304	USA	Chamber
Kade_ImnavaitCreek3_Ch	Imnavait Creek	heath	68.607	-149.296	USA	Chamber
Kim_Coldfoot1_Ch	Coldfoot	Young Black Spruce	67.183	-150.297	USA	Chamber
Kim_Coldfoot2_Ch	Coldfoot	Young Black Spruce	67.18	-150.31	USA	Chamber
Kim_Council_Ch	Council, AK	tundra sphagnum,tundra lichen,tundra tussock	64.861	-163.711	USA	Chamber

Kim_Fairbanks1_Ch	Fairbanks	Old Black Spruce	65.644	-147.471	USA	Chamber
Kim_Fairbanks2_Diff	Fairbanks	black spruce forest	64.867	-147.85	USA	Diffusion through snow
Kim_InteriorAlaska1_Ch	Interior Alaska	Gold Creek White Spruce	67.74	-149.76	USA	Chamber
Kim_InteriorAlaska2_Ch	Interior Alaska	Lower Yukon Black Spruce	65.84	-149.65	USA	Chamber
Kim_InteriorAlaska3_Ch	Interior Alaska	Upper Yukon Black Spruce	66.08	-150.17	USA	Chamber
Kim_NorthSlope1_Ch	North Slope	Subalpine tundra	68.175	-149.441	USA	Chamber
Kim_NorthSlope2_Ch	North Slope	Upland tundra	68.905	-148.876	USA	Chamber
Kim_NorthSlope3_Ch	North Slope	Subalpine tundra	68.18	-149.44	USA	Chamber
Kim_NorthSlope4_Ch	North Slope	Upland tundra	68.9	-148.88	USA	Chamber
Kim_NorthSlope5_Ch	North Slope	Coastal tundra	69.84	-148.71	USA	Chamber
Kim_SouthBrooksRange1_Ch	South Brooks Range	Tundra-boreal ecotone	67.991	-149.76	USA	Chamber
Kim_SouthBrooksRange2_Ch	South Brooks Range	Tundra-boreal ecotone	67.99	-149.76	USA	Chamber
Kljun_CA-Ojp_tower3	Saskatchewan - Western Boreal, Mature Jack Pine	CA-Ojp	53.91634	-104.692	Canada	Eddy covariance
Kljun_CA-sOBS_tower2	Southern Old Black Spruce	CA-sOBS	53.99	-105.12	Canada	Eddy covariance
Kolari_FI-Var_tower1	Varrio	FI-Var	67.7549	29.69014	Finland	Eddy covariance
Kutzbach_RU-LRD1_tower1	Samoylov Island	RU-Sam	72.37398	126.4967	Russia	Eddy covariance
Kutzbach_RU-Sam_tower1	Samoylov Island	RU-Sam	72.37398	126.4967	Russia	Eddy covariance
Kutzbach_RU-Sam_tower2	Samoylov Island	RU-Sam	72.37037	126.4817	Russia	Eddy covariance
Kutzbach_Samoylov_Tower_3_closedpath	Samoylov Island	RU-Sam	72.37382	126.4958	Russia	Eddy covariance
Kutzbach_Samoylov_Tower_3_openpath	Samoylov Island	RU-Sam	72.37382	126.4958	Russia	Eddy covariance
Kwon_US-BEO_tower2	Barrow-Bes (Biocomplexity Experiment South tower)	US-BEO	71.2809	-156.597	USA	Eddy covariance
Kwon_US-BES _tower1	Barrow-Bes (Biocomplexity Experiment South tower)	US-BES	71.281	-156.6	USA	Eddy covariance
López-Blanco_GL-NuF_tower1	Kobbefjord	GL-NuF	64.1382	-51.3784	Greenland	Eddy covariance

López-Blanco_GL-ZaF_tower1	Zackenberg	GL-ZaF	74.48143	-20.5545	Greenland	Eddy covariance
Lafleur_CA-DL1_tower1	Daring Lake	CA-DL1	64.8689	-111.575	Canada	Eddy covariance
Lafleur_CA-DL3_tower3	Daring Lake	CA-DL3	64.8722	-111.549	Canada	Eddy covariance
Lafleur_CA-DL4_tower4	Daring Lake	CA-DL4	64.8631	-111.65	Canada	Eddy covariance
Lafleur_CA-Iqa_tower1	Iqaluit	CA-Iqa	63.79025	-68.5601	Canada	Eddy covariance
Lafleur_CA-Pin_tower1	Pond Inlet	CA-Pin	72.69275	-77.9576	Canada	Eddy covariance
Larsen_Abisko1_Ch	Abisko		68.35	18.81667	Sweden	Chamber
Larsen_Abisko2_Ch	Abisko	Abisko Scientific Research Station	68.3	18.82	Sweden	Chamber
Laurila_FI-Kns_tower1	Kalevansuo	FI-Kns	60.64683	24.35617	Finland	Eddy covariance
Laurila_FI-Let_tower1	Lettosuo	FI-Let	60.64183	23.95952	Finland	Eddy covariance
Laurila_FI-Lom_tower1	Lompolojankka	FI-Lom	67.99724	24.20918	Finland	Eddy covariance
Leffler_YKD_Ch	Yukon-Kuskokwim Delta	Tutakoke River	61.25	-165.62	USA	Chamber
Lindroth_SE-Fla_tower1	Flakaliden	SE-Fla	64.11278	19.45694	Sweden	Eddy covariance
Lindroth_SE-Kno_tower1	Knottåsen	SE-Kno	60.99825	16.21728	Sweden	Eddy covariance
Lindroth_SE-Nor_tower1	Norunda	SE-Nor	60.0865	17.4795	Sweden	Eddy covariance
Lund_DK-ZaH_tower1	Zackenberg	DK-Zah, Heath	74.47328	-20.5503	Greenland	Eddy covariance
Maanavilja_Kaamanen_Ch	Kaamanen		69.13333	27.28333	Finland	Chamber
Machimura_RU-Nel_tower1	Nelegel	RU-Nel	62.31583	129.4997	Russia	Eddy covariance
Margolis_CA-Obs_tower1	Saskatchewan - Western Boreal, Mature Black Spruce	CA-Obs	53.98717	-105.118	Canada	Eddy covariance
Margolis_CA-Qfo_tower1	Quebec - Eastern Boreal, Mature Black Spruce	CA-Qfo	49.6925	-74.3421	Canada	Eddy covariance
Marushchak_Seida_Ch	Seida	Upland Tundra Heath,Dry Peatlands, Wetlands	67.05	62.93333	Russia	Chamber
Mastepanov_Zackenberg_Ch	Zackenberg	fen	74.479	-20.555	Greenland	Chamber
Maximov_RU-Elg_tower1	Elgeeii	RU-Elg	60.016	133.824	Russia	Eddy covariance

Maximov_RU-SkP_tower1	Yakutsk Spasskaya Pad larch	RU-SkP	62.255	129.168	Russia	Eddy covariance
McCaughey_CA-Gro_tower1	Ontario - Groundhog River, Boreal Mixedwood Forest	CA-Gro	48.2167	-82.1556	Canada	Eddy covariance
McCaughey_CA-Man_tower1	Manitoba - Northern Old Black Spruce (former BOREAS Northern Study Area)	CA-Man	55.87962	-98.4808	Canada	Eddy covariance
Merbold_RU-Che_tower1	Cherskiy	RU-Che	68.61304	161.3414	Russia	Eddy covariance
Miyazaki_MO-UFRS_tower1	Mongolia	MO-UFRS	48.27333	106.8508	Mongolia	Eddy covariance
Mkhabela_CA-OJP_tower4	Saskatchewan - Western Boreal, Mature Jack Pine	CA-Ojp	53.916	-104.69	Canada	Eddy covariance
Mkhabela_CA-SF1_tower1	Saskatchewan - Western Boreal, forest burned in 1977	CA-SF1	54.48503	-105.818	Canada	Eddy covariance
Mkhabela_CA-SF2_tower2	Saskatchewan - Western Boreal, forest burned in 1989	CA-SF2	54.25392	-105.878	Canada	Eddy covariance
Mkhabela_CA-SF3_tower3	Saskatchewan - Western Boreal, forest burned in 1998	CA-SF3	54.09156	-106.005	Canada	Eddy covariance
Mkhabela_HJP02_tower7	HJP02 Jack Pine	CA-HJP02	53.15	-104.1	Canada	Eddy covariance
Mkhabela_HJP75_tower5	HJP75 Jack Pine	CA-HJP75	53.15	-104.1	Canada	Eddy covariance
Mkhabela_HJP94_tower6	HJP94 Jack Pine	CA-HJP94	53.15	-104.117	Canada	Eddy covariance
Morgner_Adventdalen_Ch	Adventdalen, Svalbard	heath control,meadow control	78.167	16.067	Norway	Chamber
Nakai_US-Prr_tower1	Poker Flats	US-Prr	65.12367	-147.488	USA	Eddy covariance
Nielsen_Abisko_Ch	Abisko	Wet NE-facing slope	68.35	18.81667	Sweden	Chamber
Nilsson_SE-Deg_tower1	Degerö	SE-Deg	64.18203	19.55654	Sweden	Eddy covariance
Olivas10_Utqia?vik_Ch	Utqia?vik North,Utqia?vik South,Utqia?vik Central	North,South,Central	71.32	-156.62	USA	Chamber
Olivas11_Utqia?vik_Ch	Utqia?vik	Vascular-dominated,Intermediate,Polygon Rim	71.32	-156.62	USA	Chamber
Parmentier_NO-And_tower1	Andøya	NO-And	69.14278	16.02222	Norway	Eddy covariance
Pirk_Adventdalen_Diff	Adventdalen, Svalbard	Advent-fen, active low center ice wedge polyons	78.183	15.917	Norway	Diffusion through snow
Pirk_Zackenberg_Ch	Zackenberg	fen	74.5	-21	Greenland	Chamber
Pirk_Zackenberg_Diff	Zackenberg	fen	74.5	-21	Greenland	Diffusion through snow

Poyatos_Petsikko_Ch	Petsikko	Several hummocks and hollows	69.35983	27.23136	Finland	Chamber
Rebmann_RU-Zot_tower1	Zotino	RU-Zot	60.8008	89.3507	Russia	Eddy covariance
Rocha_US-An1_tower1	Anaktuvuk River Severe Burn	US-An1	68.99	-150.28	USA	Eddy covariance
Rocha_US-An2_tower2	Anaktuvuk River Moderate Burn	US-An2	68.95	-150.21	USA	Eddy covariance
Rocha_US-An3_tower3	Anaktuvuk River Unburned	US-An3	68.93	-150.27	USA	Eddy covariance
Schuur_EML_Ch	Eight Mile Lake	minimal thaw,moderate thaw,extensive thaw	63.88306	-149.226	USA	Chamber
Schuur_US-EML_tower1	Eight Mile Lake	US-EML	63.8784	-149.254	USA	Eddy covariance
Semenchuk_Adventdalen_Ch	Adventdalen, Svalbard	dry heath	78.167	16.067	Norway	Chamber
Shaver_US-ICh_tower1	Imnavait Creek Watershed	US-ICh	68.6068	-149.296	USA	Eddy covariance
Sonnentag_CA-SMC_tower1	Smith Creek	CA-SMC	63.153	-123.252	Canada	Eddy covariance
Sonnentag_CA-TVC_tower1	Trail Valley Creek	CA-TVC	68.74617	-133.502	Canada	Eddy covariance
Startsev_Anzac_Ch	Mackenzie Valley, Anzac, Mid-Boreal - Peat Plateau,MacKenzie Valley, Anzac, Mid-Boreal - Upland	mid boreal - peat plateau,mid boreal - upland	56.4	-111.03	Canada	Chamber
Startsev_FortSimpson_Ch	Mackenzie Valley, Fort Simpson, High Boreal - Peat Plateau,Mackenzie Valley, Fort Simpson, High Boreal - Upland	boreal forest - peat plateau ,boreal forest - upland	61.63	-121.4	Canada	Chamber
Startsev_Inuvik_Ch	Mackenzie Valley, Inuvik, High Sub-Arctic - Peat Plateau,Mackenzie Valley, Inuvik, High Sub-Arctic - Upland	high subarctic - peat plateau,high subarctic - upland	68.32	-133.43	Canada	Chamber
Startsev_NormanWells_Ch	Mackenzie Valley, Normal Wells, Low Sub-Arctic - Peat Plateau,Mackenzie Valley, Norman Wells, Low Sub-Arctic - Upland	low subarctic - peat plateau,low subarctic - upland	65.21	-127.01	Canada	Chamber
Startsev_NormanWells_Ch	Mackenzie Valley, Norman Wells, Low Sub-Arctic - Upland	low subarctic - upland	65.21	-127.01	Canada	Chamber
Strachan_CA-LLC_tower1	Lac Le Caron (hereafter referred to as LLC) peatland, an ombrotrophic bog	CA-LLC	52.29028	-75.2542	Canada	Eddy covariance
Strebel_Adventdalen_Ch	Adventdalen, Svalbard		78.167	16.1	Norway	Chamber
Sullivan_AgashashokRiver_Diff	Agashashok River, Noatak National Preserve	NTL, treeline low density spruce,STL, treeline low density white	67.48	-162.2	USA	Diffusion through snow

		spruce,SNE, white spruce forest,NSE, white spruce forest,NNE, white spruce forest,SSE, white spruce forest,TER, low density white spruce				
Sullivan_ToolikLake1_Diff	Toolik Lake	tussock tundra	68.62	-149.605	USA	Diffusion through snow
Sullivan_ToolikLake2_Diff	Toolik Lake	dry heath tundra	68.622	-149.598	USA	Diffusion through snow
Sullivan_ToolikLake3_Diff	Toolik Lake	wet sedge tundra	68.625	-149.6	USA	Diffusion through snow
Sullivan_ToolikLake4_Diff	Toolik Lake	riparian willow tundra	68.626	-149.596	USA	Diffusion through snow
Sullivan_ToolikLake5_Diff	Toolik Lake	dwarf birch tundra	68.632	-149.573	USA	Diffusion through snow
Syed_CA-WP1_tower1	Alberta - Western Peatland - LaBiche River,Black Spruce/Larch Fen	CA-WP1	54.95384	-112.467	Canada	Eddy covariance
TornDengel_US-NGB_tower1	NGEE Arctic Barrow	US-NGB	71.28333	-156.616	USA	Eddy covariance
TornDengel_US-NGC_tower1	NGEE Arctic Council	US-NGC	64.85196	-163.7	USA	Eddy covariance
Tuittila_FI-Sii_tower1	Siikaneva	FI-Sii	61.83265	24.19285	Finland	Eddy covariance
Uchida_Svalbard_Ch	E. Brogger Glacier		79	12	Norway	Chamber
Ueyama_US-CR-Fire_tower1	Cascaden Ridge Fire Scar	US-Fcr	65.39678	-149.121	USA	Eddy covariance
Vesala_FI-Hyy_tower1	Hyytiala	FI-Hyy	61.84741	24.29477	Finland	Eddy covariance
Voigt_Seida_Ch	Northeast Russia	bare peat,peat plateau,upland tundra	67.05	62.91667	Russia	Chamber
Voigt_Seida_Ch	Northeast Russia	bare peat	67.05	62.91667	Russia	Chamber
Waldrop_BonanzaCreek_Diff	Bonanza Creek	Sphagnum bog	64.69	-148.32	USA	Diffusion through snow
Welp_US-Bn1_tower1	Delta Junction	Populus tremuloides; understory: salix; Epilobium angustifolium and Festuca altaica	63.90111	-145.373	USA	Eddy covariance

Welp_US-Bn2_tower2	Delta Junction	US-Bn2	63.88806	-145.739	USA	Eddy covariance
Wickland_BonanzaCreek_Ch	Bonanza Creek	permafrost plateau PP,thermokarst wetland TW	64.41	-148.19	USA	Chamber
Zona_US-Atq_tower1	Atqasuk	US-Atq	70.4696	-157.409	USA	Eddy covariance
Zona_US-Brw_tower1	Barrow Environmental Observatory (BEO) tower	US-Brw	71.281	-156.596	USA	Eddy covariance
Zona_US-Brw_tower2	Barrow-Bes (Biocomplexity Experiment South tower)	US-Brw	71.281	-156.596	USA	Eddy covariance
Zona_US-Brw_tower3	Barrow	US-Brw	71.323	-156.609	USA	Eddy covariance
Zona_US-Ivo_tower1	Ivotuk	US-Ivo	68.4865	-155.75	USA	Eddy covariance
Zyryanov_RU_IG_tower1	Igarka	RU-IG	67.4812	86.43727	Russia	Eddy covariance
Zyryanov_RU_Tura_tower1	Tura; Nizhnyaya Tunguska River	RU-Tur	64.20889	100.4636	Russia	Eddy covariance

Supplementary Table 3. Predictor details.

Data product and name	**Spatial resoluti on**	**Temporal resolution and period: Static, Monthly (or higher), Annual**	**Quality flags**	**Model (1 km or 8 km)**	**Reference**	**Mechanism for driving the flux**
TerraClimate meteorological variables: air temperature , vapor pressure deficit, and solar radiation	1/24°, ~4 km	Monthly 1/1958->	-	1 and 8 km	[35]	Air temperatures control enzymatic processes and thus GPP and R_{eco} [36,37]. Vapor pressure deficit is linked to GPP: higher moisture levels increase GPP [38]. GPP is dependent on solar radiation (and in particular diffuse radiation) as a resource for photosynthesis [39].
Day-time land surface	1 km	Monthly from 2/2000->	We used bit 0-1 value	1 km	[40]	Surface temperatures are more tightly linked to vegetation and soil conditions

temperature MOD11A2v006			<=1: Pixel produced, unreliable or unquantifiable quality, recommend examination of more detailed QA			than air temperatures and control enzymatic processes and thus GPP and R_{eco} [41]
ERA5 land soil moisture and temperature at 0-5 cm depth, snow cover	0.1°, ~9 km	Monthly from 1/1950->	-	1 and 8 km	[42,43]	Soil moisture is an important resource for GPP and regulates R_{eco} ; drier soils often have higher R_{eco} than water-saturated soils [44]. Soil temperatures control soil respiration which can occur at temperatures lower than 0 C and can contribute to R_{eco} up to 70% [24,45]. Snow cover reflects both the amount of snow, and timing of snowmelt and snowfall which are important drivers of not only winter but also growing season fluxes [46,47].
Barrow atmospheric CO2 concentrations	Assuming one location represents the entire atmosphere	Monthly from 1/1973	-	1 and 8 km	[48]	Increasing CO_2 concentrations (CO_2 fertilization) accelerate GPP[49]
ESA CCI vegetation type + Circumpolar Arctic Vegetation Map (CAVM) vegetation type	1 km (ESA CCI originally 300 m; CAVM 1 km)	Static	-	1 and 8 km	Following [3] based on ESA CCI (2017) and [50]	Vegetation composition and structure are important drivers of CO_2 fluxes [51] and also act as a surrogate for many other environmental conditions (e.g., soil wetness, soil nutrients). Classes included in our vegetation type map are: barren and prostrate shrub tundra, graminoid tundra, shrub tundra, wetland, sparse boreal vegetation, needleleaved evergreen tree cover, broadleaved deciduous tree cover, needleleaved deciduous tree cover, mosaic and mixed vegetation type.
NDVI MOD13A1v006	500 m	Monthly from 2/2000->	We used SummaryQA bit 0-1 value 0 together with value 1 with smaller weights	1 km	[52]; gap-filled and smoothed with weighted Whittaker & constant lambda approach [9]	NDVI represents vegetation greenness and productivity patterns, and is a widely used vegetation index that is strongly correlated with GPP and partly also R_{eco} and NEE [53,54].
GIMMS3g NDVI	ca. 8 km	Monthly from 7/1981 to 12/2017 (with recent updates up to 2022)	We used data covering all the flags 0-2; poorer-quality data used only to gap-fill high-quality data	8 km	[55]	See above.
MOD44B	250 m	Annual from	-	1 km	[56]	Vegetation cover is linked to the amount

Percent Tree Cover, Percent Non-Tree Cover, Percent Non-Vegetated Cover		2000->				of green biomass and thus CO_2 fluxes [57]
AVHRR VCF5KYR Percent Tree Cover, Percent Non-Tree Cover, Percent Non-Vegetated Cover	Ca. 5.6 km	Annual from 1982 to 2016	-	8 km	[58]	See above.
SoilGrids v2 variables: pH (water solution) at the topsoil (0-5 cm), soil organic carbon stock in the uppermost 2 m	250 m	Static	-	1 and 8 km	[59,60]	Soil pH may be associated with soil nutrient content and thus regulates the availability of resources for plants and microbes (lower pH potentially correlates with stronger net CO_2 sinks [61]). Soil organic carbon stock describes the amount of material available for decomposition and may thus be correlated with R_{eco} [62].
Topographic indices calculated from MERIT DEM: compound topographic index (CTI)	250 m	Static	-	1 and 8 km	[63]	CTI is a topographic index that describes the accumulation of water in topographic depressions (synonym to topographic wetness index), and might thus be correlated with GPP and R_{eco} [64].
Permafrost probability	1 km	Static	-	1 and 8 km	[65]	Permafrost protects organic matter from decomposition and thus defines how much material is available for decomposition in the soil [66].

Supplementary Table 4.

	GPP	Reco	NEE
Sample size for 1 km model	3869	3869	4765
Sample size for 8 km model	3968	3970	4897

Supplementary Table 5. Model performance based on different subsets of data for the 1-km models.

Flux	Model training data	Performance estimates
NEE	All data	RMSE 15.9 R2 0.66 MAE 12.6
NEE	Eddy covariance only	RMSE 17.5 R2 0.69 MAE 13.7
NEE	Non-disturbed sites only	RMSE 14.6 R2 0.66 MAE 11.5
GPP	All data	RMSE 35.0 R2 0.82 MAE 27.2
GPP	Eddy covariance only	RMSE 32.3 R2 0.87 MAE 24.4
GPP	Non-disturbed sites only	RMSE 35.2 R2 0.79 MAE 28.0
Reco	All data	RMSE 28.9 R2 0.74 MAE 23.4
Reco	Eddy covariance only	RMSE 27.5 R2 0.76 MAE 21.5
Reco	Non-disturbed sites only	RMSE 28.0 R2 0.70 MAE 23.2

Supplementary Table 6. Details related to the process and inversion models included in the model intercomparison. The number of assimilated sites in the inversions in the Arctic-boreal region varies from ca. 10 up to 30 over the study period. At large scales, the inversions that have priors (i.e., prior values given by a process model; included in four out of five inversions) are hardly constrained by the priors but at regional scales and in areas with poor data coverage (e.g., Siberia), the posterior flux might be reflecting the prior flux.

Model type	Model name	Details and reference

Atmospheric inversions	CAMS	Release v21r1 of the inversion produced by the Copernicus Atmosphere Monitoring Service (https://atmosphere.copernicus.eu/), driven by air-sample measurements and included in the Global Carbon Budget 2022; total land CO2 flux adjusted for fossil fuel emissions, cement carbonation sink, and lateral fluxes[67].
Atmospheric inversions	sEXTocNEET	Contribution to the Global Carbon Budget 2022; total land CO2 flux adjusted for fossil fuel emissions, cement carbonation sink, and lateral fluxes[67]
Atmospheric inversions	CTE	Contribution to the Global Carbon Budget 2022; driven by atmospheric observations in Obspack Globalviewplus v7.0 and NRT v7.2 [68]; total land CO2 flux adjusted for fossil fuel emissions, cement carbonation sink, and lateral fluxes[67]
Atmospheric inversions	NISMON	Contribution to the Global Carbon Budget 2022; total land CO2 flux adjusted for fossil fuel emissions, cement carbonation sink, and lateral fluxes[67]
Atmospheric inversions	UoE	Contribution to the Global Carbon Budget 2022; total land CO2 flux adjusted for fossil fuel emissions, cement carbonation sink, and lateral fluxes[67]
Process models: coupled CMIP6 models	ACCESS-ESM1-5	Based on historical model runs with model outputs from 2001 to 2014 [29]
Process models: coupled CMIP6 models	BCC-ESM1	Based on historical model runs with model outputs from 2001 to 2014 [29]
Process models: coupled CMIP6 models	BCC-CSM2-MR	Based on historical model runs with model outputs from 2001 to 2014 [29]

Process models: coupled CMIP6 models	CanESM5	Based on historical model runs with model outputs from 2001 to 2014 [29]
Process models: coupled CMIP6 models	CESM2	Based on historical model runs with model outputs from 2001 to 2014 [29]; CESM2 includes permafrost carbon in the model
Process models: coupled CMIP6 models	CMCC-ESM2	Based on historical model runs with model outputs from 2001 to 2014 [29]
Process models: coupled CMIP6 models	CNRM-ESM2	Based on historical model runs with model outputs from 2001 to 2014 [29]
Process models: coupled CMIP6 models	GFDL-ESM4	Based on historical model runs with model outputs from 2001 to 2014 [29]
Process models: coupled CMIP6 models	IPSL-CM6A	Based on historical model runs with model outputs from 2001 to 2014 [29]
Process models: coupled CMIP6 models	MIROC-ES2L	Based on historical model runs with model outputs from 2001 to 2014 [29]
Process models: coupled CMIP6 models	MPI-ESM1-2-LR	Based on historical model runs with model outputs from 2001 to 2014 [29]
Process models: coupled CMIP6 models	NorESM2-LM	Based on historical model runs with model outputs from 2001 to 2014 [29]; NorESM2-LM includes permafrost carbon in the model
Process models: coupled CMIP6 models	UKESM1-0-LL	Based on historical model runs with model outputs from 2001 to 2014 [29]

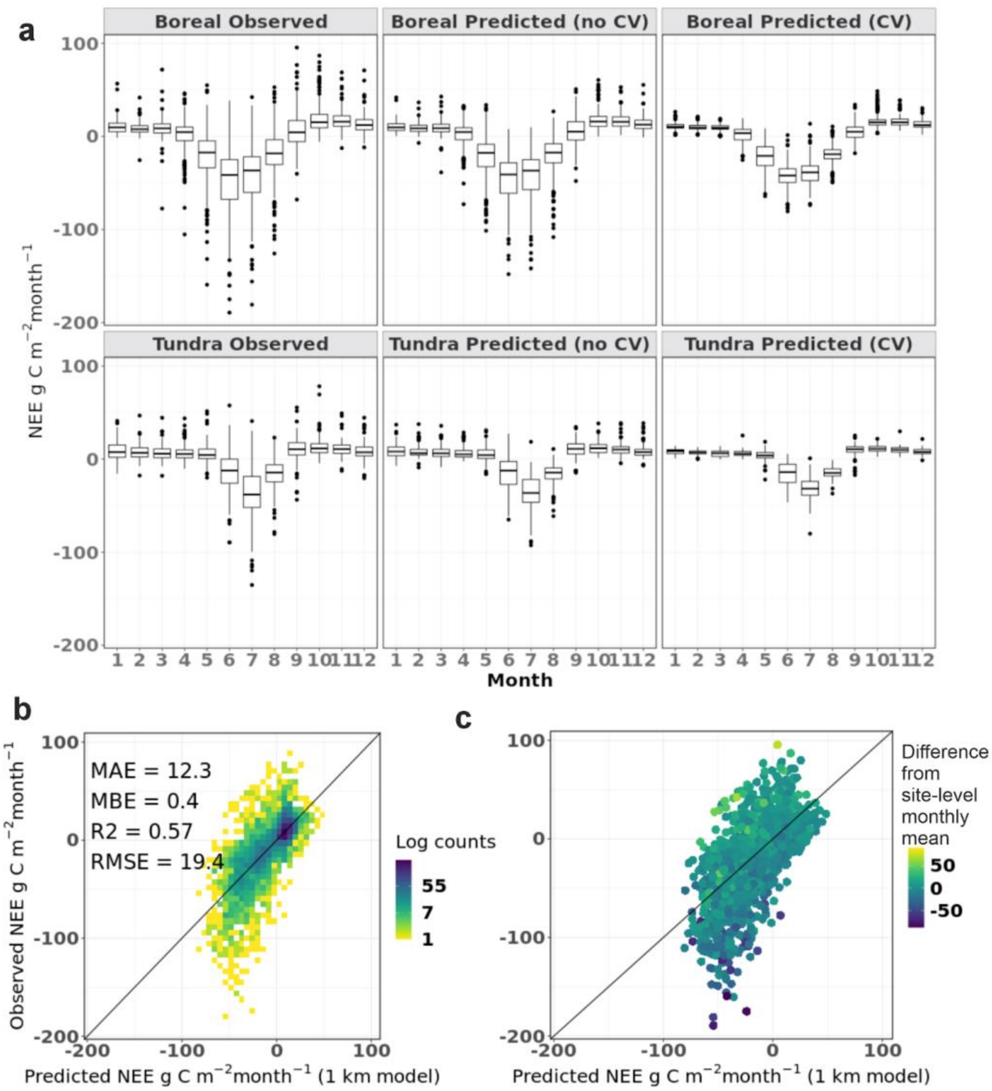

Supplementary Fig 1. Predictive performance of the NEE model estimated using leave-one-site-out approach. Colors in subplot c indicate deviance from average site-level monthly flux and indicate that the model struggles the most when observations from individual sites have a large deviance from the mean.

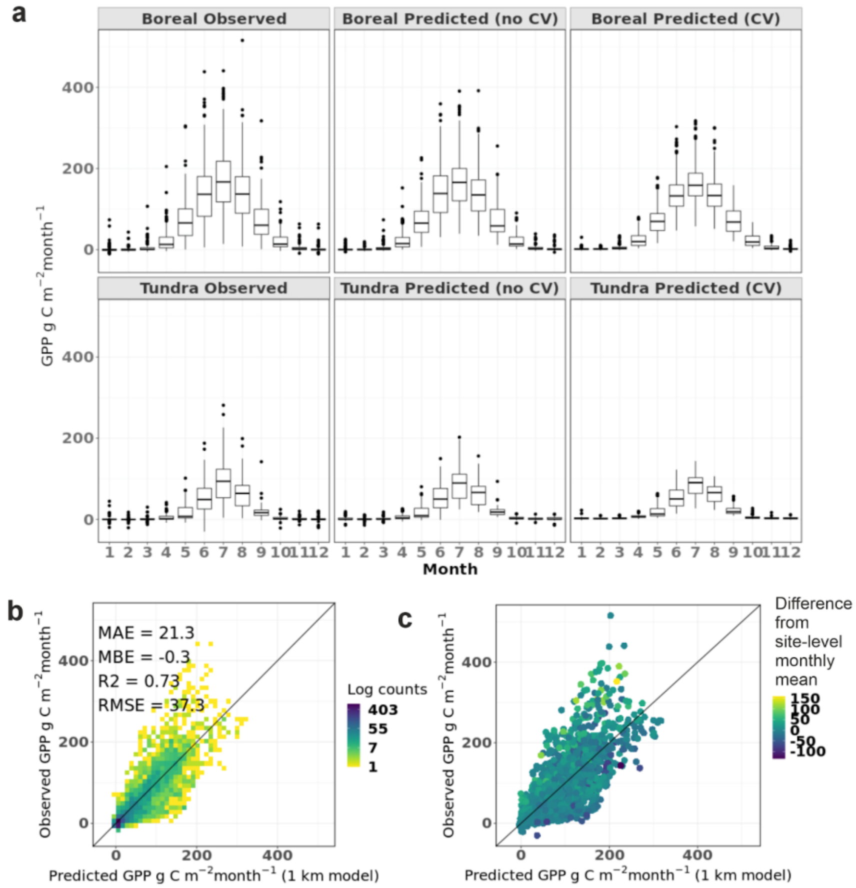

Supplementary Fig 2. Predictive performance of the GPP model estimated using leave-one-site-out approach.

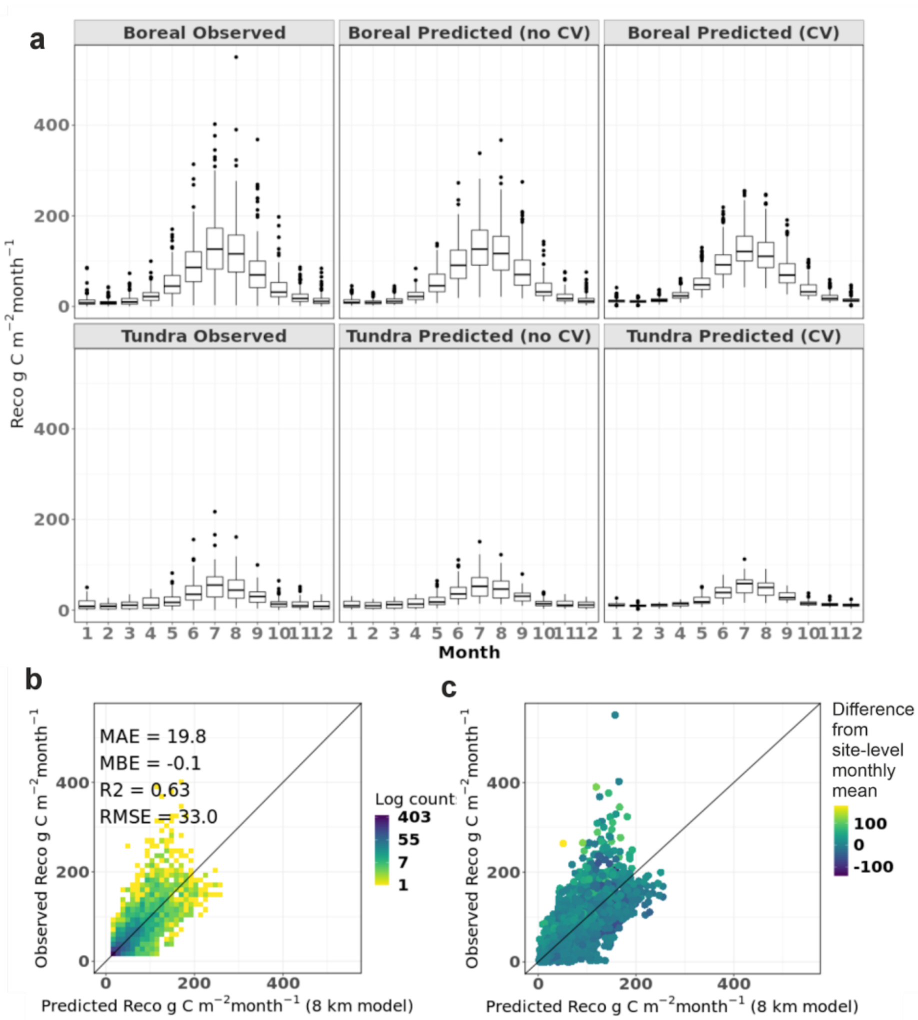

Supplementary Fig 3. Predictive performance of the R_{eco} model estimated using leave-one-site-out approach.

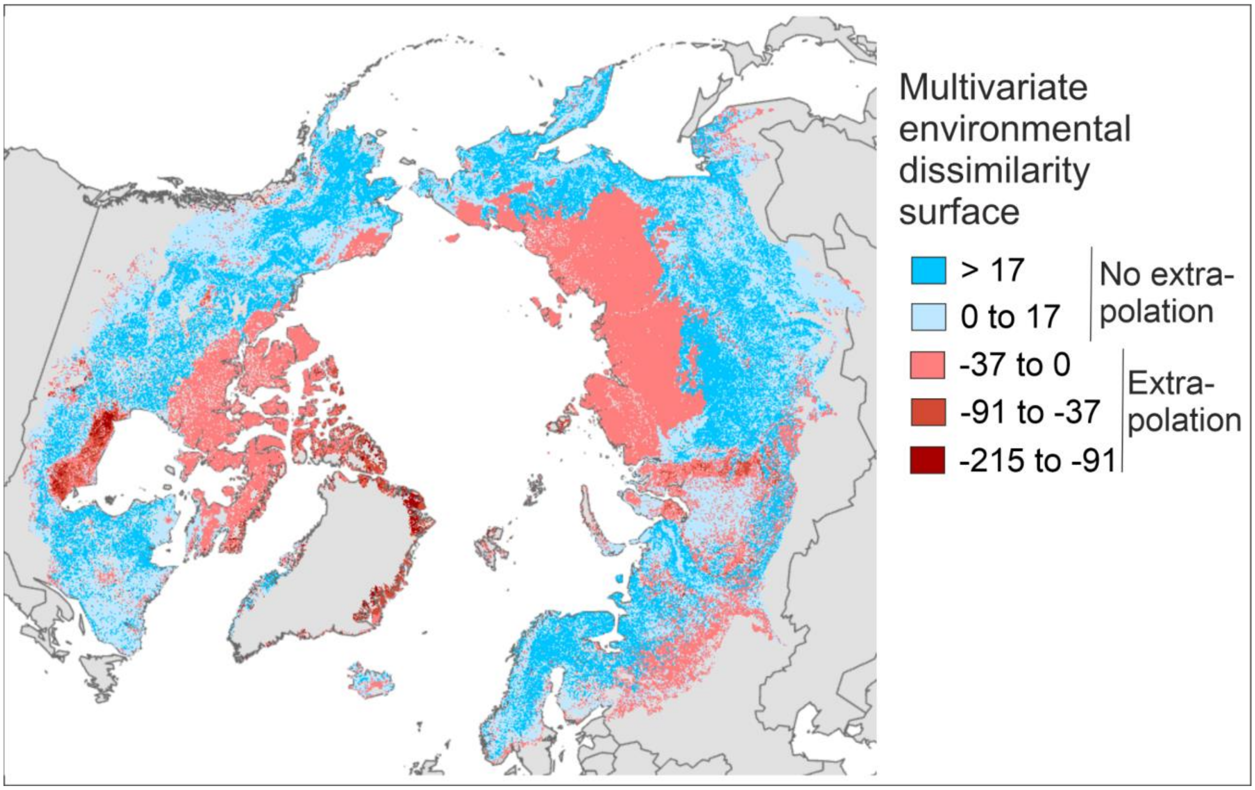

Supplementary Fig. 4. Maps showing the area of extrapolation for NEE models based on sites that have data at least from one January (i.e., year-round sites).

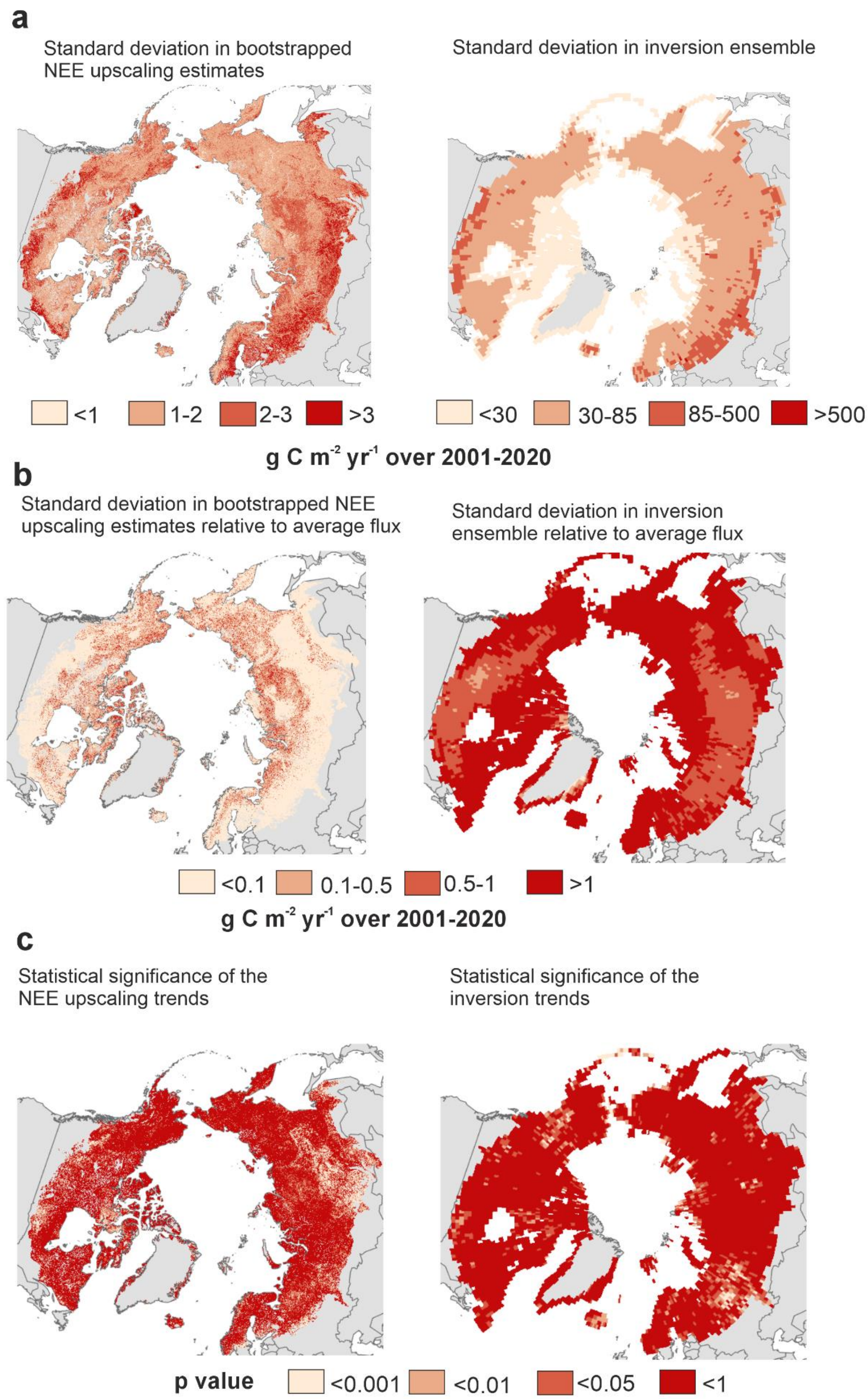

468
469 Supplementary Fig. 5. Uncertainties for the upscaled and inversion NEE.

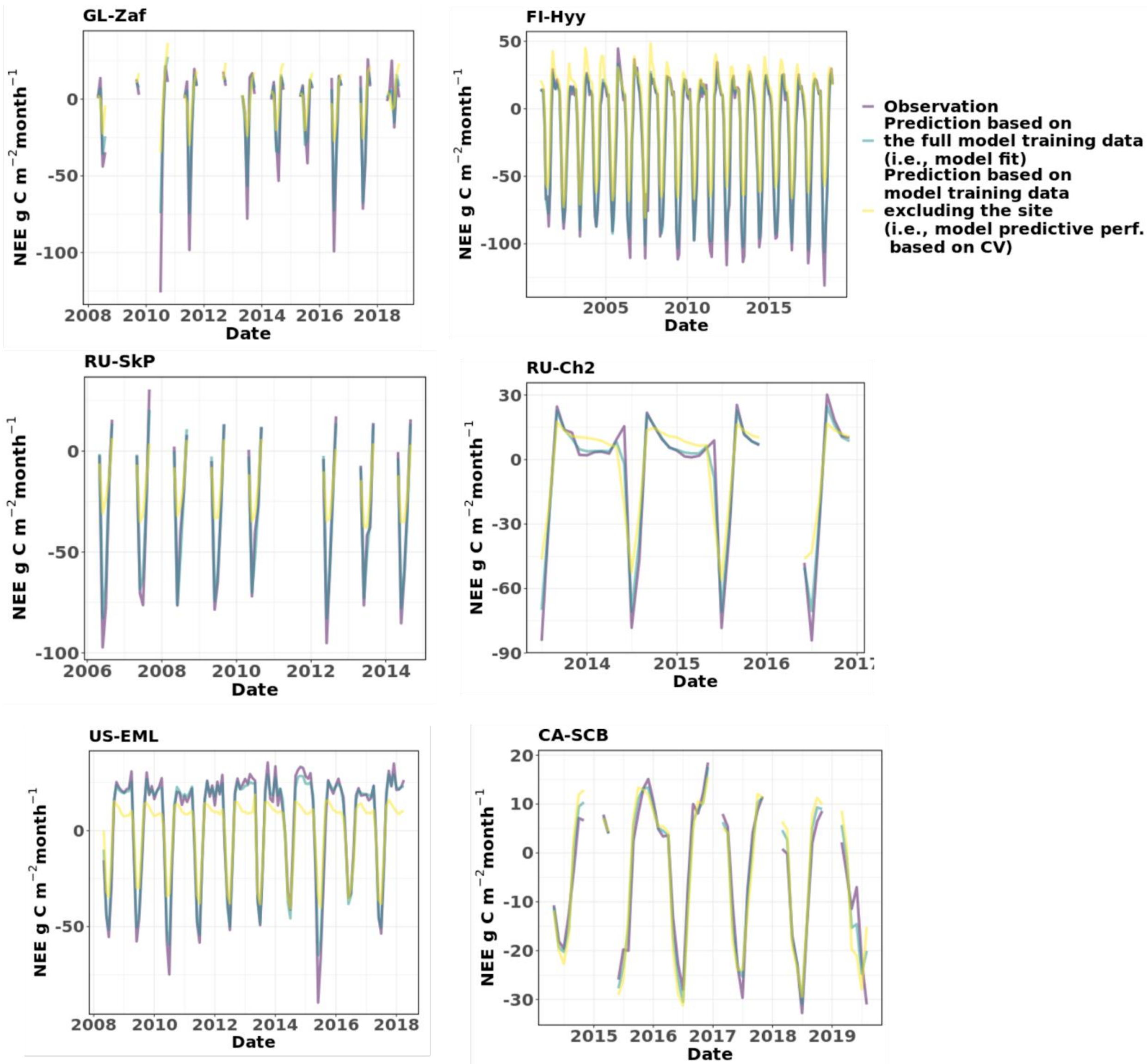

Supplementary Fig. 6. Time series of NEE from a subset of sites and their agreement with model predictions. Model fit indicates how well the model trained with the entire model training data predicts to the same data and model predictive performance shows how the models perform when a dataset excluding the specific site is used to train the model.

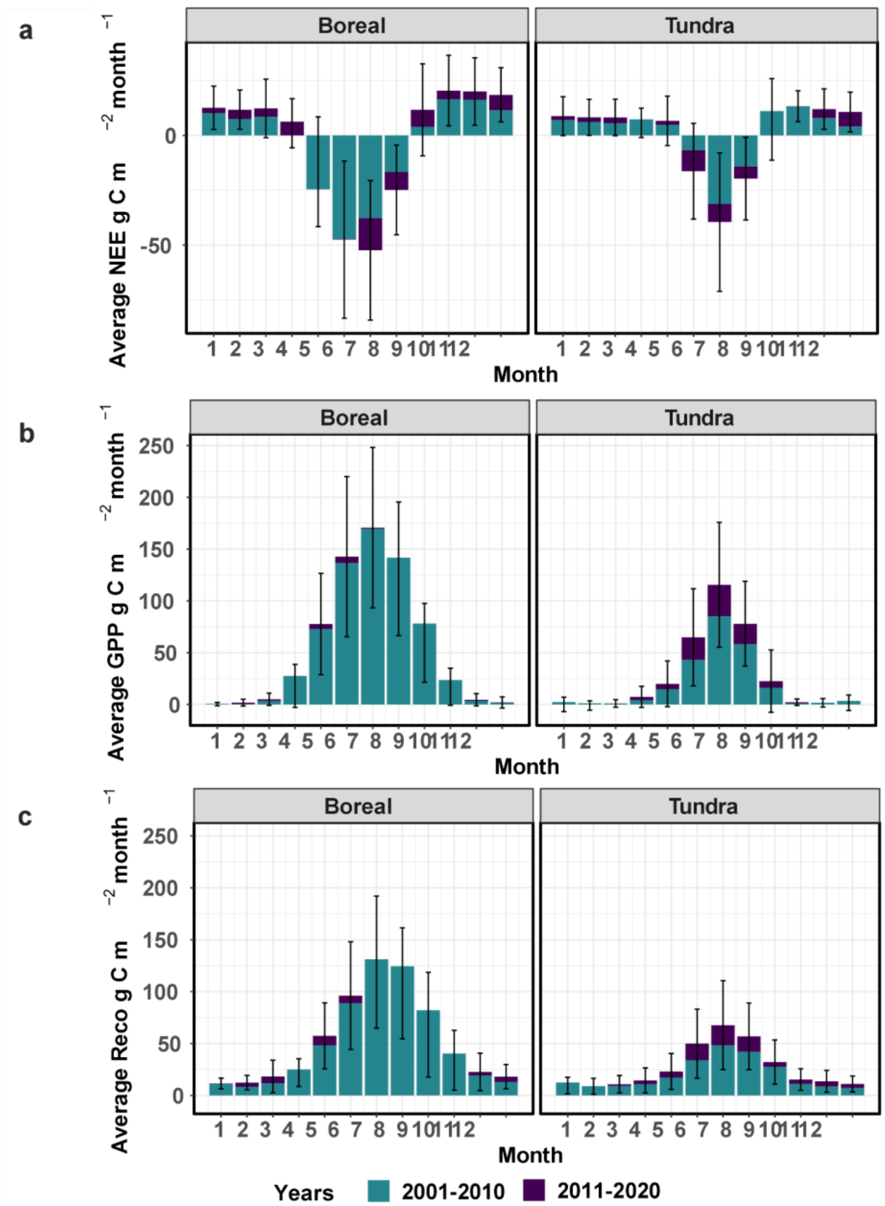

Supplementary Fig 7. Average in-situ monthly NEE, GPP, and R_{eco} in boreal and tundra biomes during the past two decades. Note that this figure is highly uncertain as it does not account for the differences in the site distribution across the two decades. Fig. 3 in the main text shows the upscaled monthly fluxes that should better represent the average fluxes across the entire ABZ.

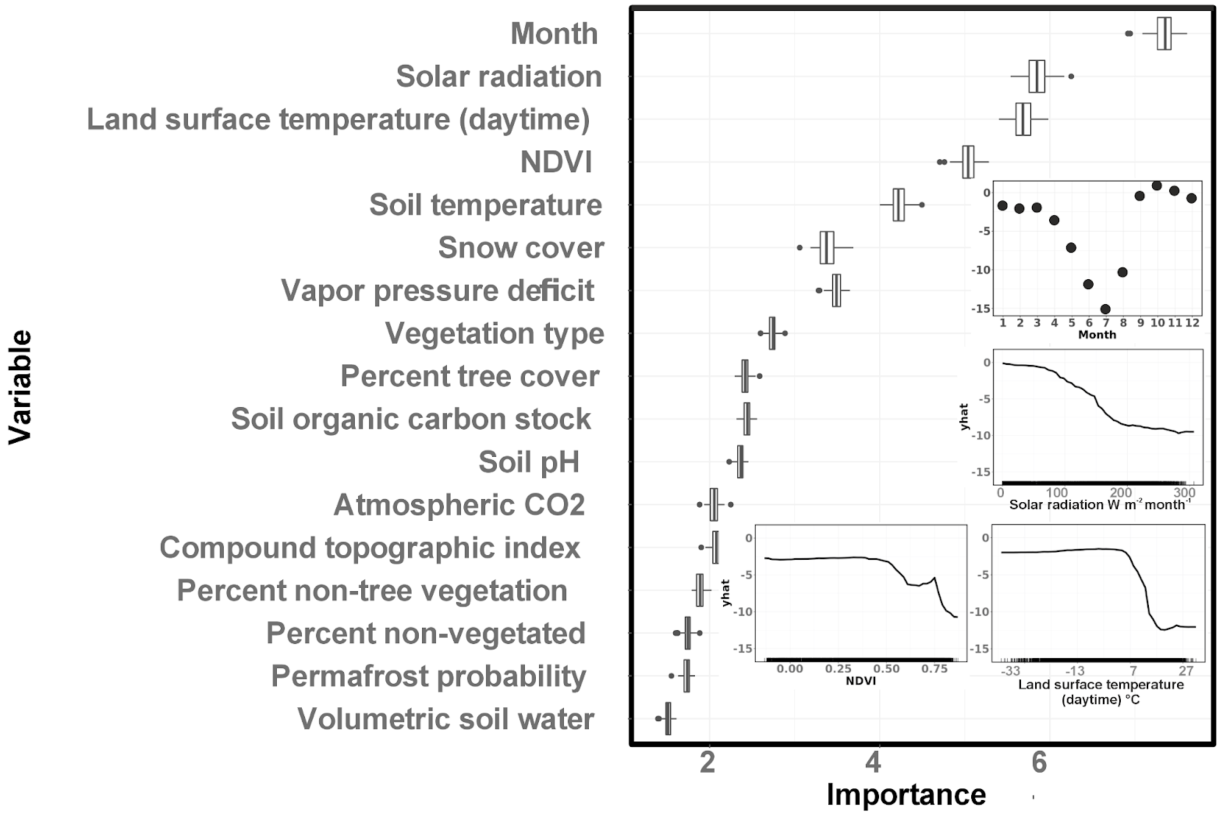

Supplementary Fig. 8. Variable importance plots and the partial dependence plots for the most important predictors of the 1-km NEE model.

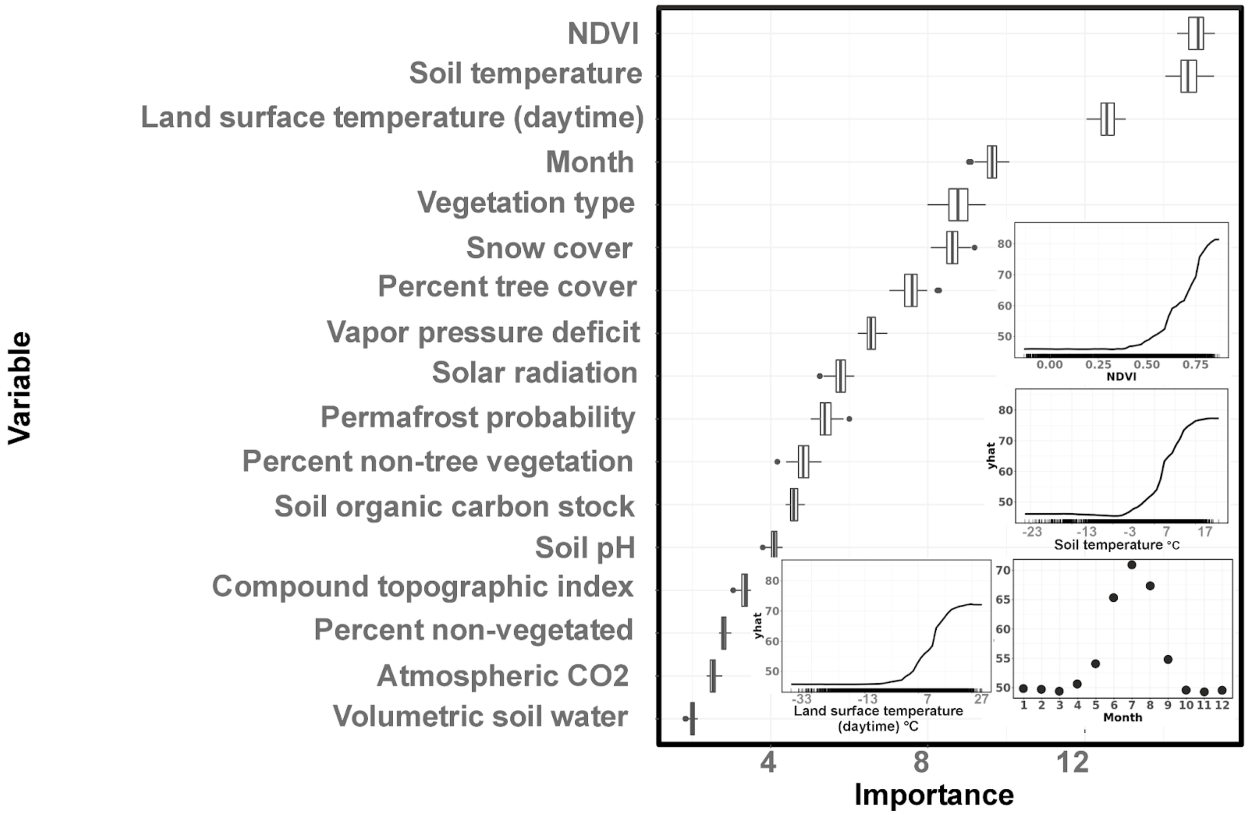

Supplementary Fig. 9. Variable importance plots and the partial dependence plots for the most important predictors of the GPP model.

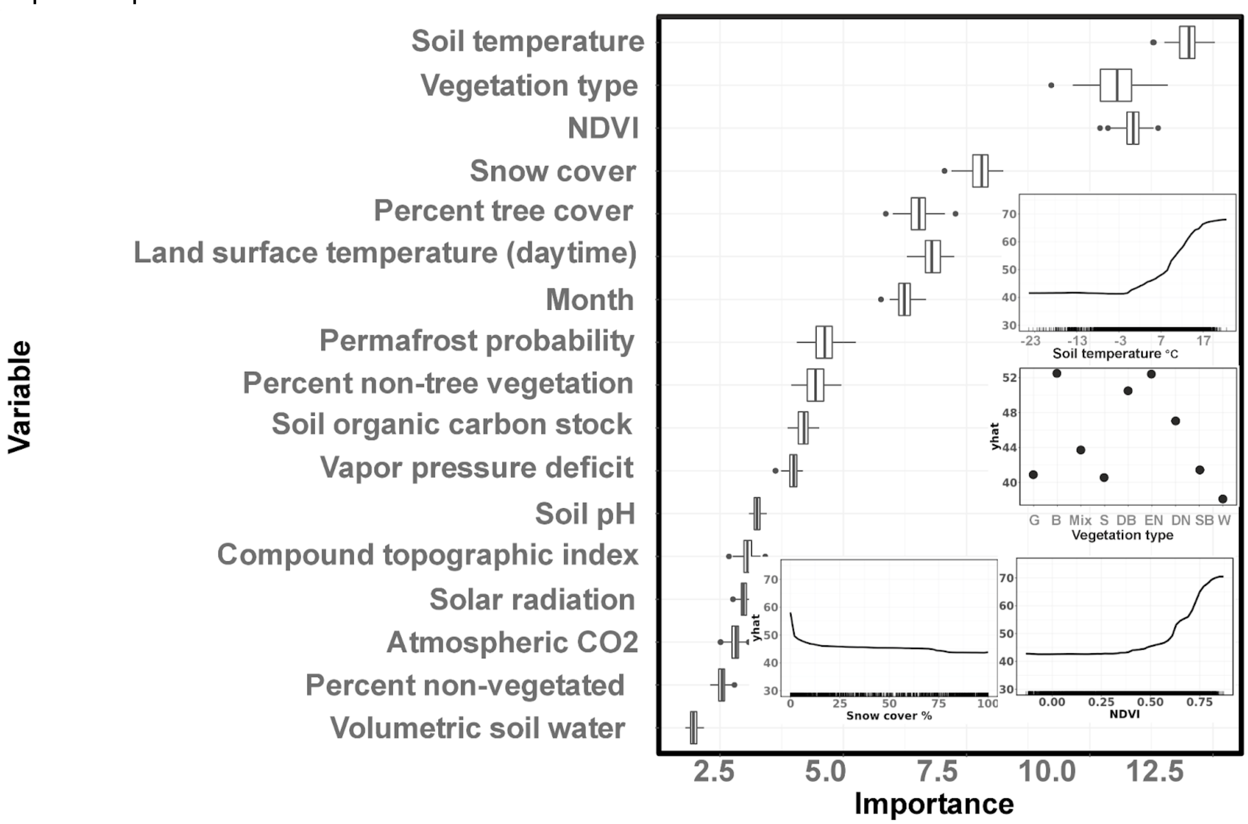

Supplementary Fig. 10. Variable importance plots and the partial dependence plots for the most important predictors of the R_{eco} model. Vegetation types include G=graminoid, B=barren, Mix=mixed forest and mosaic vegetation type, S=shrub, DB=deciduous broadleaf forest, EN=evergreen needleleaf forest, DN=deciduous needleleaf forest, SB=sparse boreal vegetation, W=wetland.

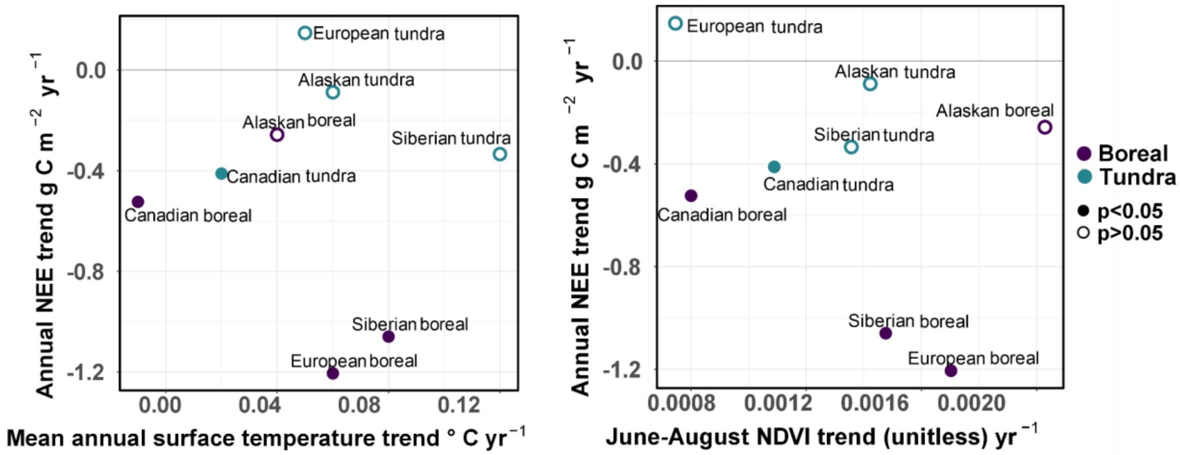

Supplementary Fig. 11. Correlation between average temperature and NDVI trends with upscaled average annual NEE trends over 2001-2020. The statistical significance of the NEE trend is shown with full and empty circles.

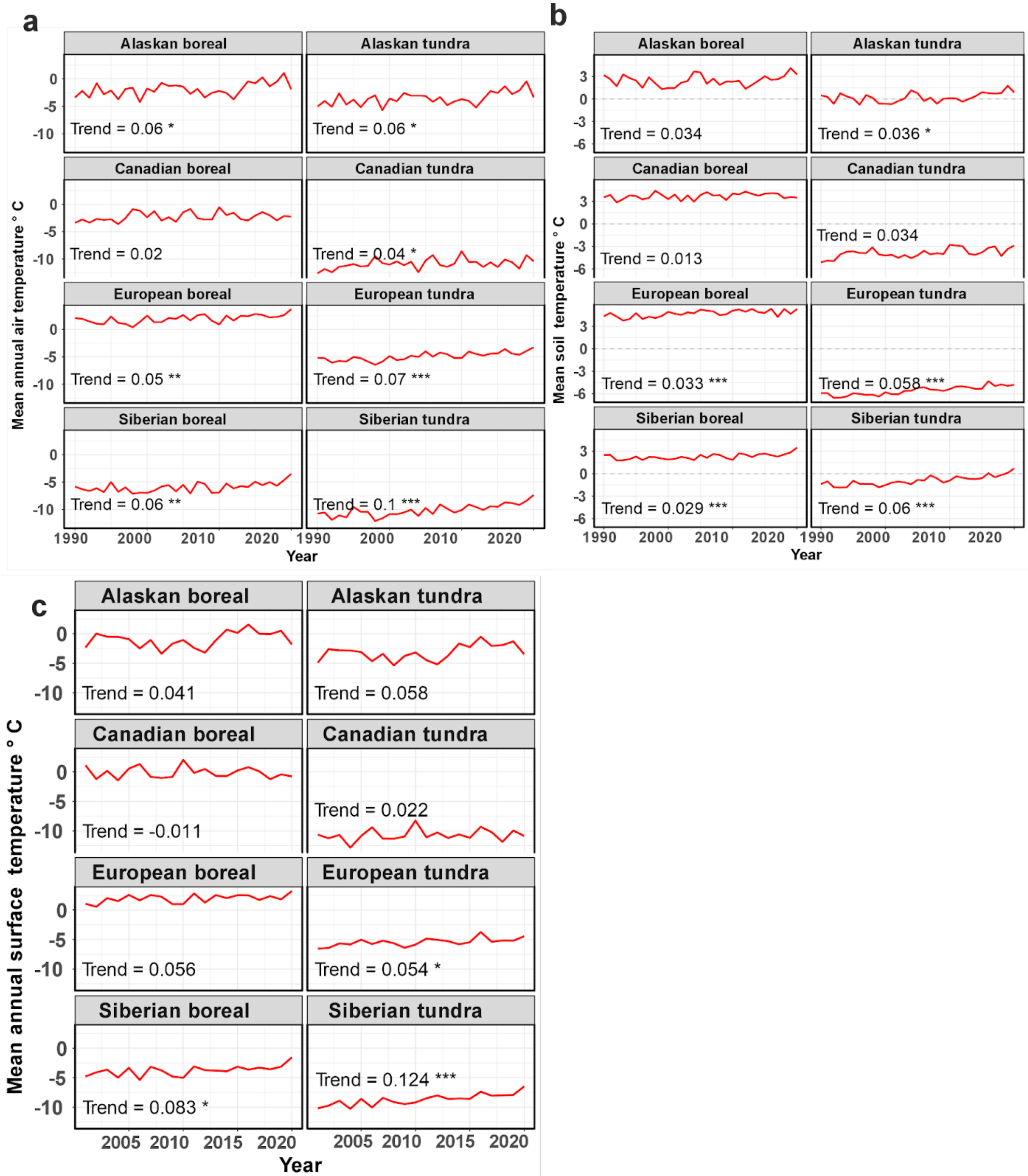

Supplementary Fig. 12. Trends (°C yr^{-1}) for the air, land surface and soil temperature variables included in the models. Figures show that all regions are showing increases in air and soil temperatures. The Siberian tundra has the strongest air and soil temperature trends whereas the Canadian boreal has the weakest non-significant trends. Stars in the trend values depict the significance of the trend (*= p<0.05, **=p<0.01, ***=p<0.001).

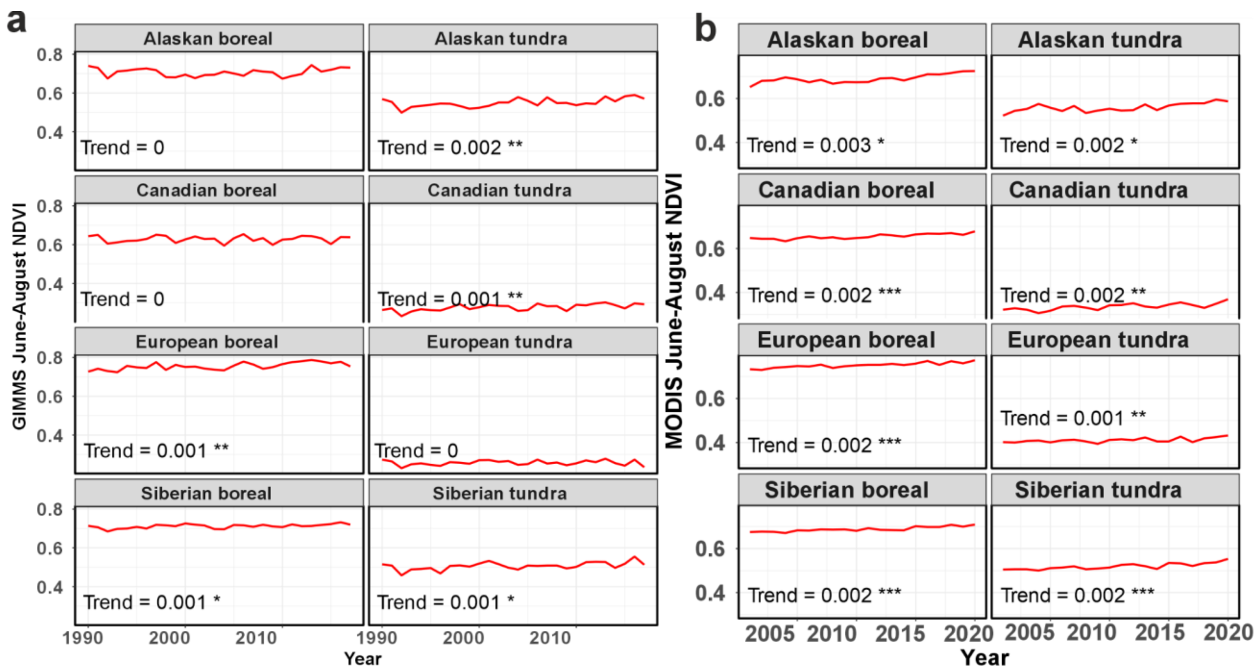

Supplementary Fig. 13. Trends for the NDVI variables for the June-August period. The GIMMS dataset used here covers a longer time period (1990-2016) but is limited to 8-km pixel resolution, whereas the MODIS NDVI time series goes from 2001 to 2020 and is at 1-km pixel resolution. Average greening trends are almost equally strong across the regions in the MODIS era but there is more variability in the GIMMS era. Weakest trends are found in European tundra across both the datasets; GIMMS shows strong trends particularly in Alaskan tundra. Stars in the trend values depict the significance of the trend (*= p<0.05, **=p<0.01, ***=p<0.001).

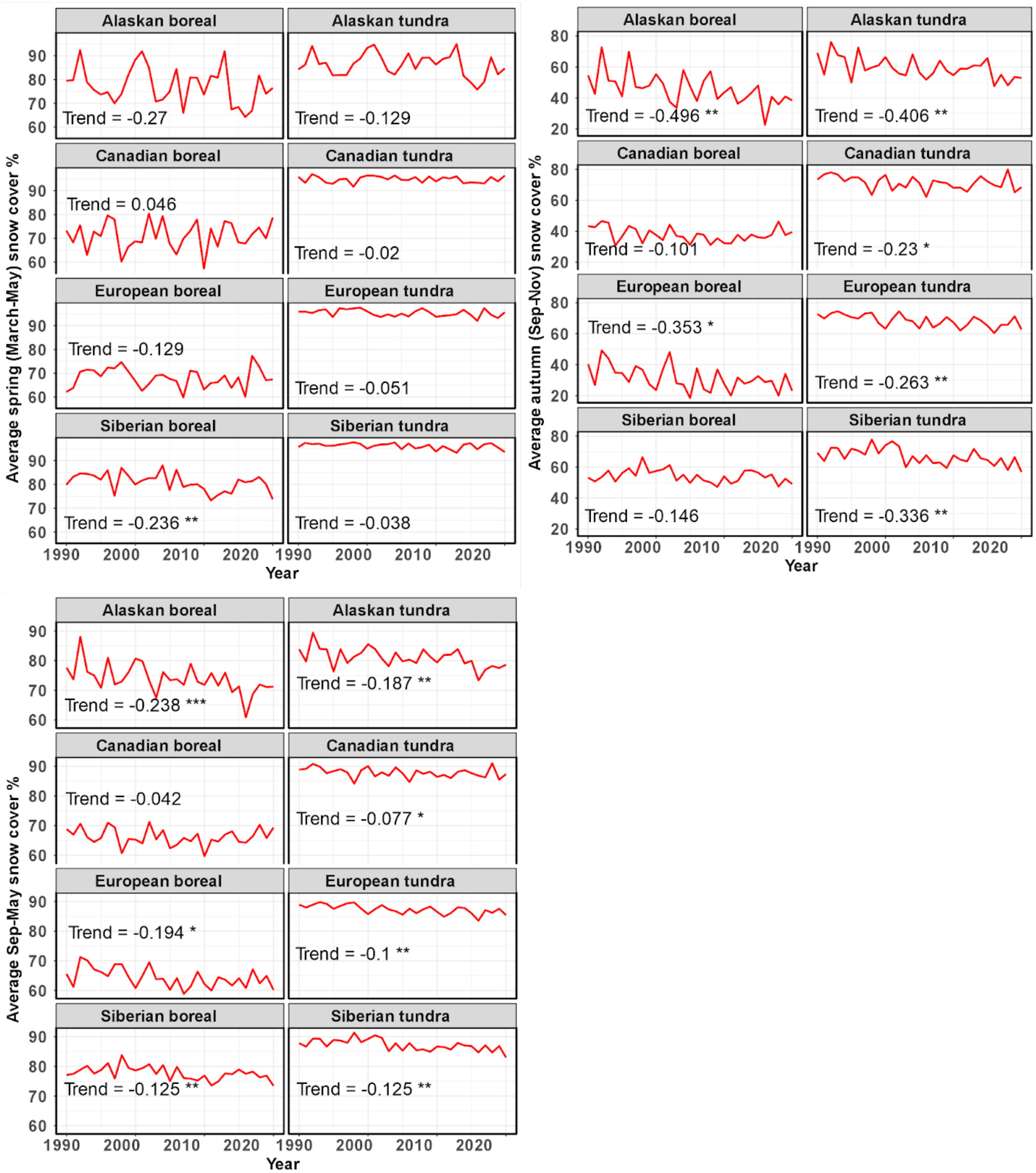

Supplementary Fig. 14. Trends ($\% \, yr^{-1}$) for the snow cover variable included in the models show that all regions experience declining snow cover in spring, autumn, and the entire non-summer (September-May) season. However, snow cover trends are stronger and statistically significant primarily in the autumn season, except for the Siberian boreal region that experiences a strong statistically significant declining trend in the spring. Declines in snow cover are the steepest in Alaskan boreal and tundra regions. Stars in the trend values depict the significance of the trend (*= p<0.05, **=p<0.01, ***=p<0.001).

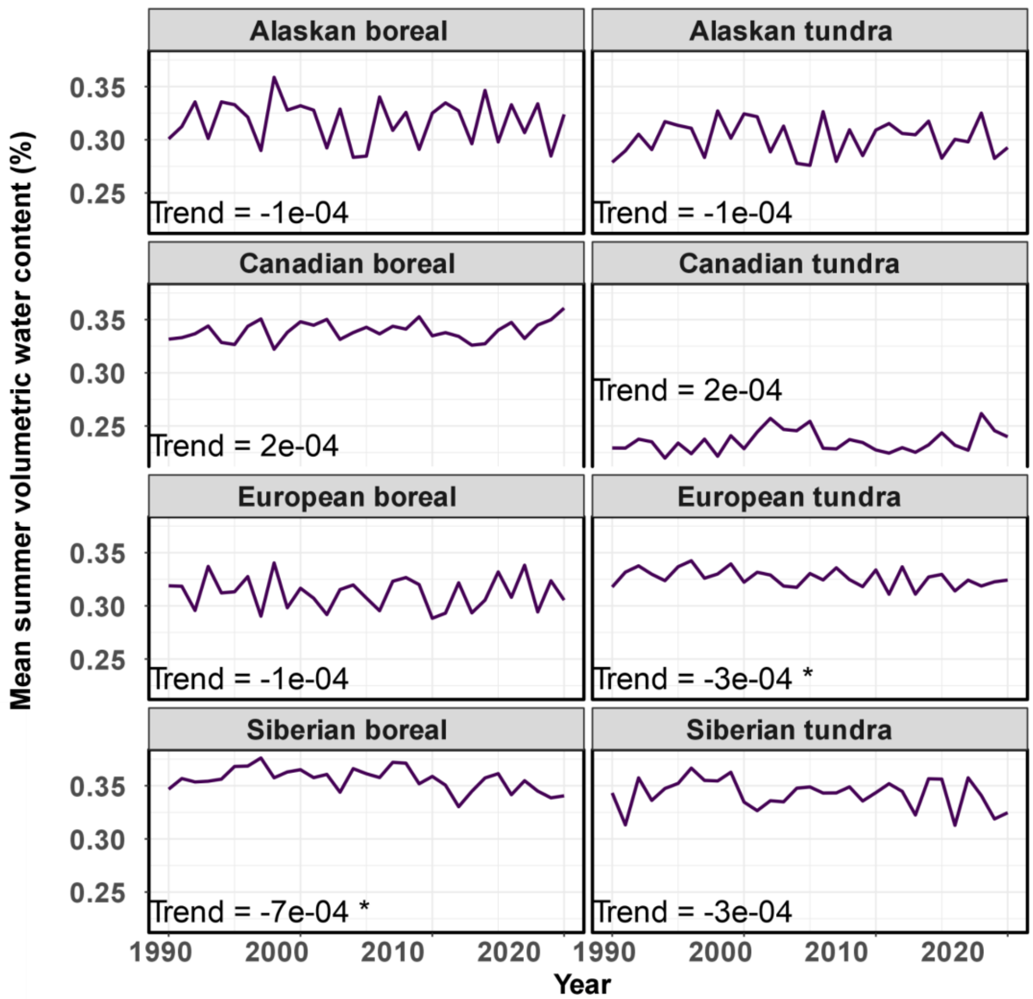

Supplementary Fig. 15. Trends (% yr^{-1}) for June-August soil moisture. Stars in the trend values depict the significance of the trend (*= p<0.05, **=p<0.01, ***=p<0.001).

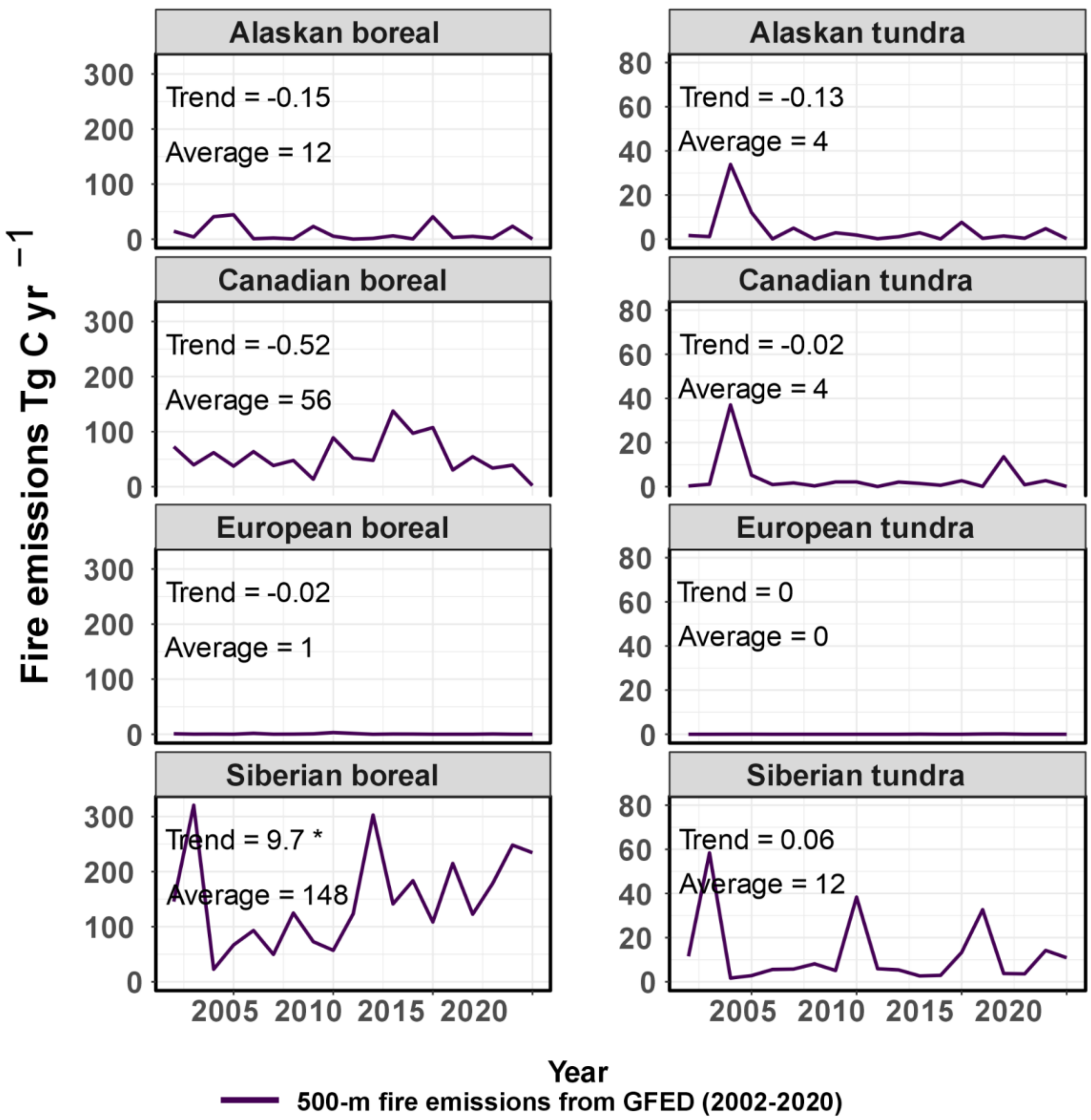

556
557 Supplementary Fig. 16. Annual fire emission budgets across the key domains. Stars in the trend
558 values depict the significance of the trend (*= p<0.05, **=p<0.01, ***=p<0.001).
559

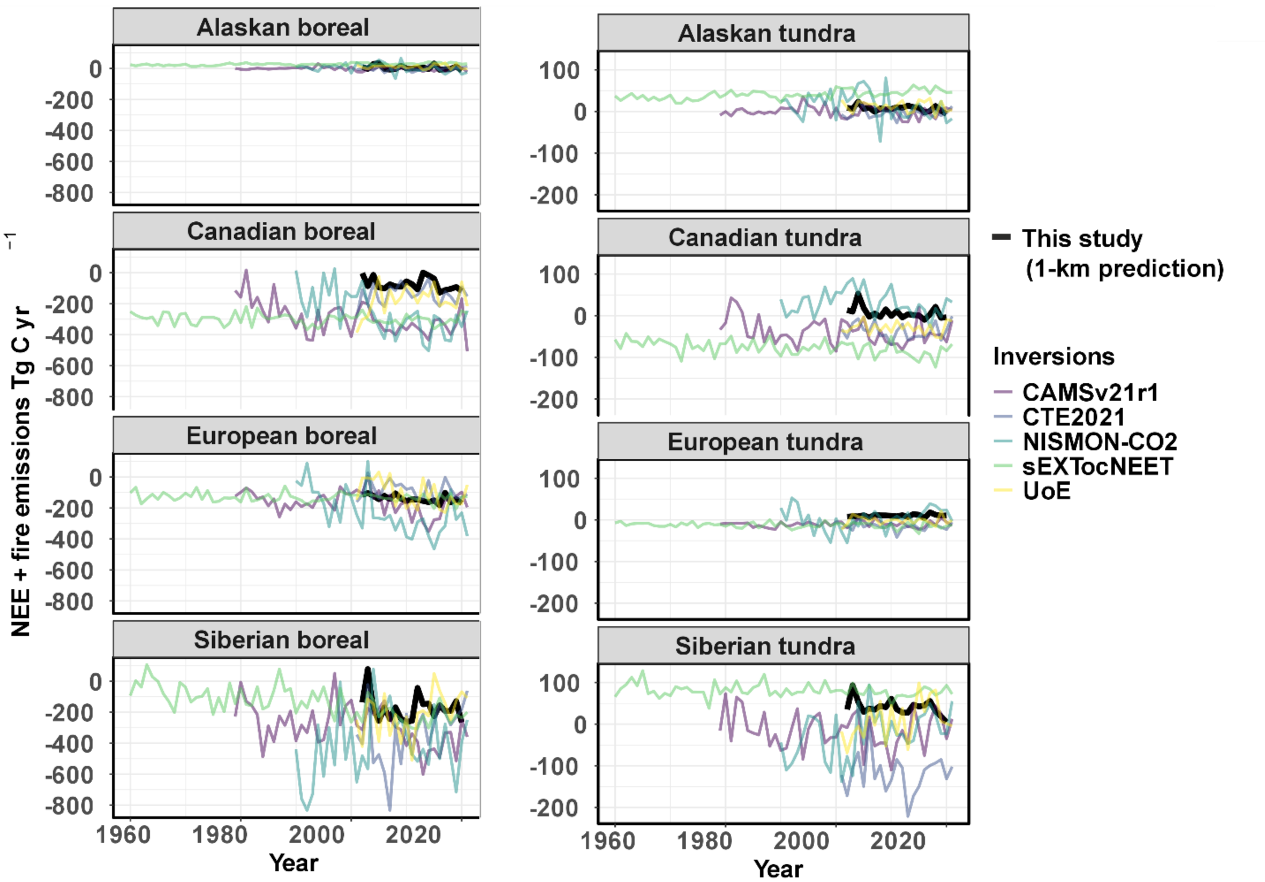

560
561 Supplementary Fig. 17. Time series of NEE + fire emissions from the 1-km predictions produced
562 in this study and the atmospheric inversions.
563
564
565
566

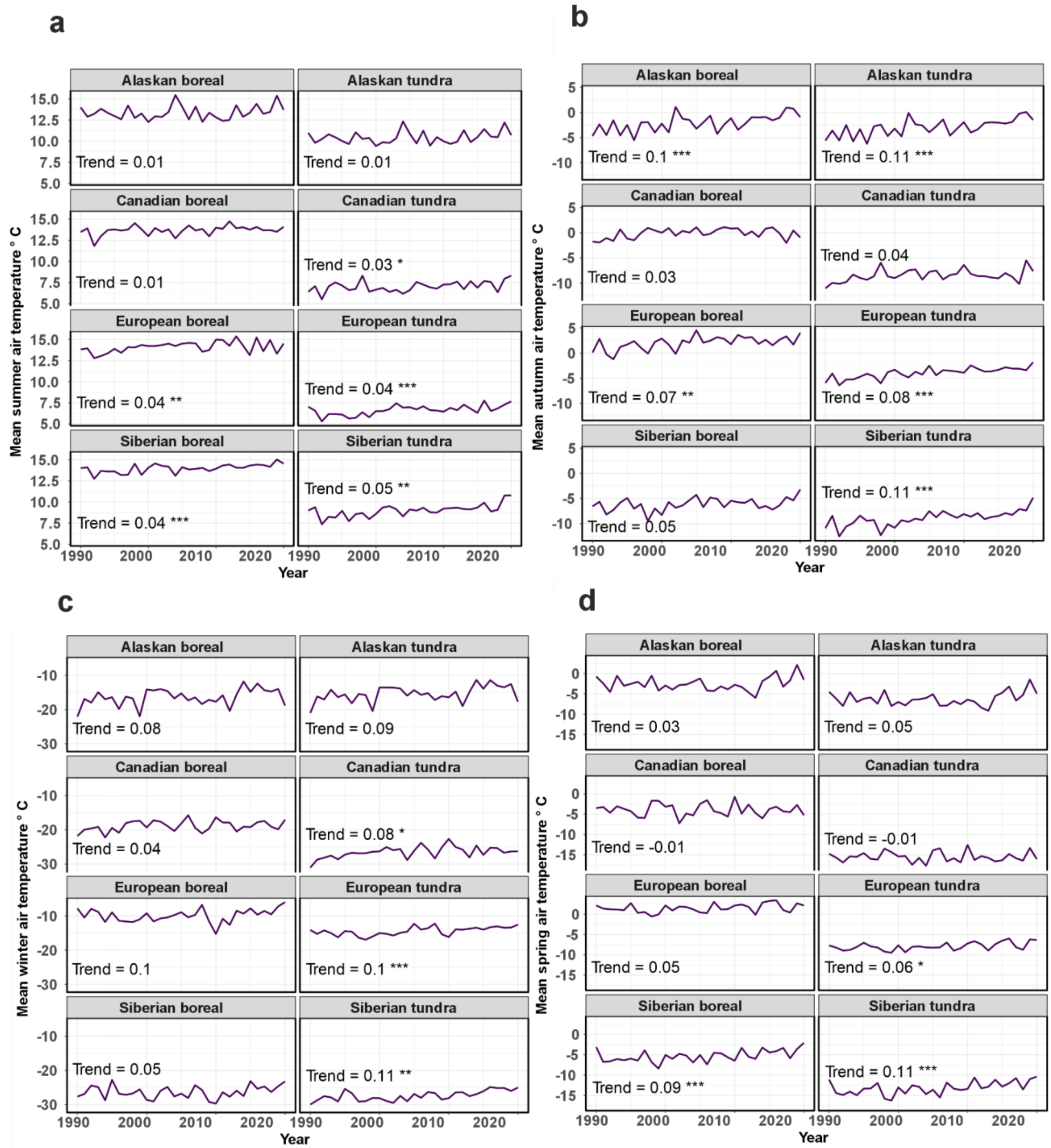

Supplementary Fig. 18. Trends (°C yr^{-1}) for the air temperature variables in different climatological seasons. Stars in the trend values depict the significance of the trend (*= p<0.05, **=p<0.01, ***=p<0.001).

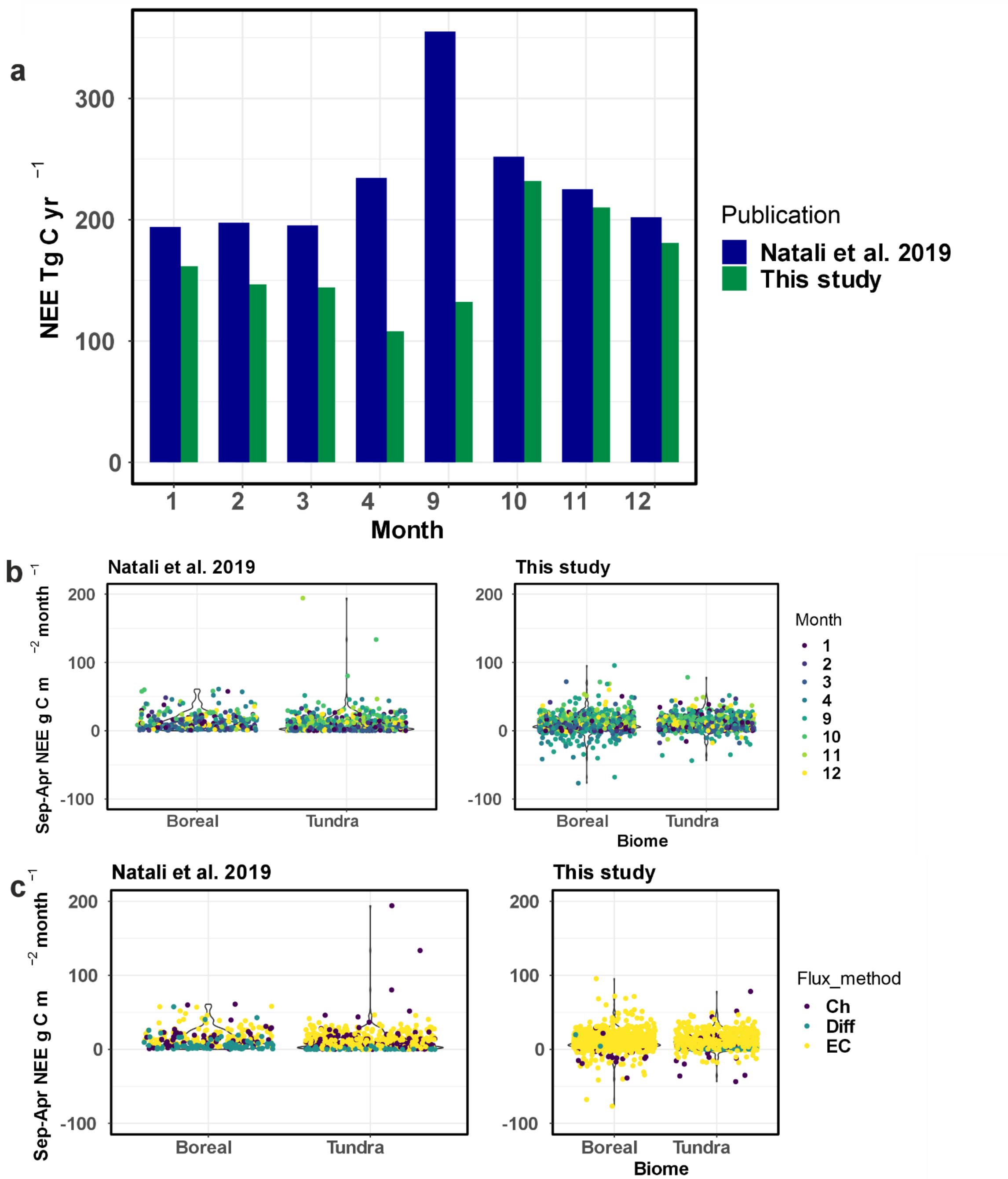

Supplementary Fig. 19. Comparison of the permafrost region non-growing season net ecosystem exchange (NEE) between Natali et al. (2019) and this study across monthly upscaled budgets (a), and in-situ monthly flux data visualized with months (b) and flux measurement methods (c). Natali et al. (2019) removed negative average monthly fluxes during the non-growing season to focus on net emissions, with a total number of site-months being 859 (in this study, site-months in the permafrost region totaled 1702). The October-April budget in this study was 1,181 Tg C yr^{-1} compared with 1,501 Tg C yr^{-1} in Natali et al. (2019) for the same period and domain.

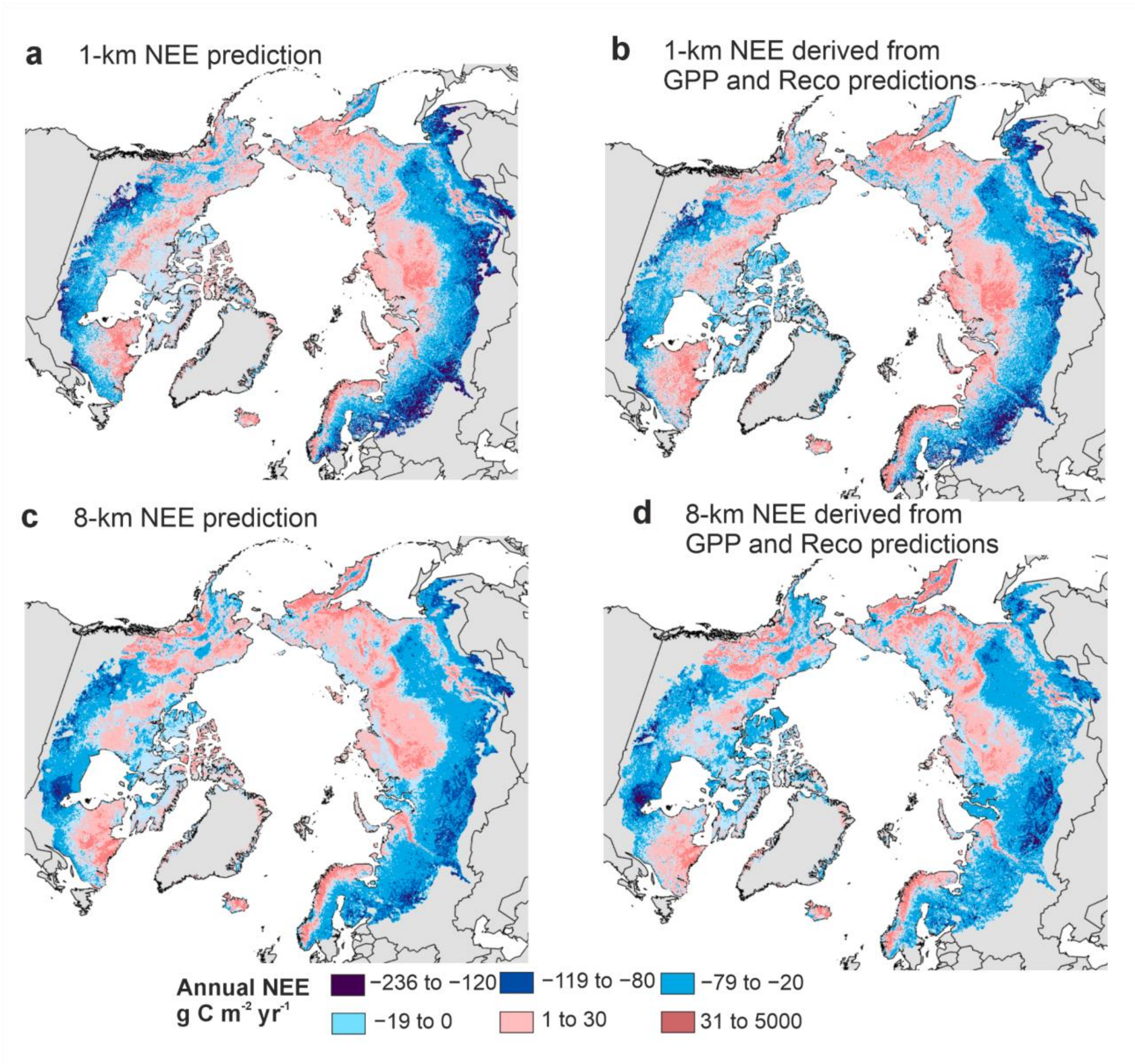

Supplementary Fig. 20. A comparison of upscaled NEE at 1 and 8-km predictions and from directly derived NEE or GPP-R_{eco} derived NEE.

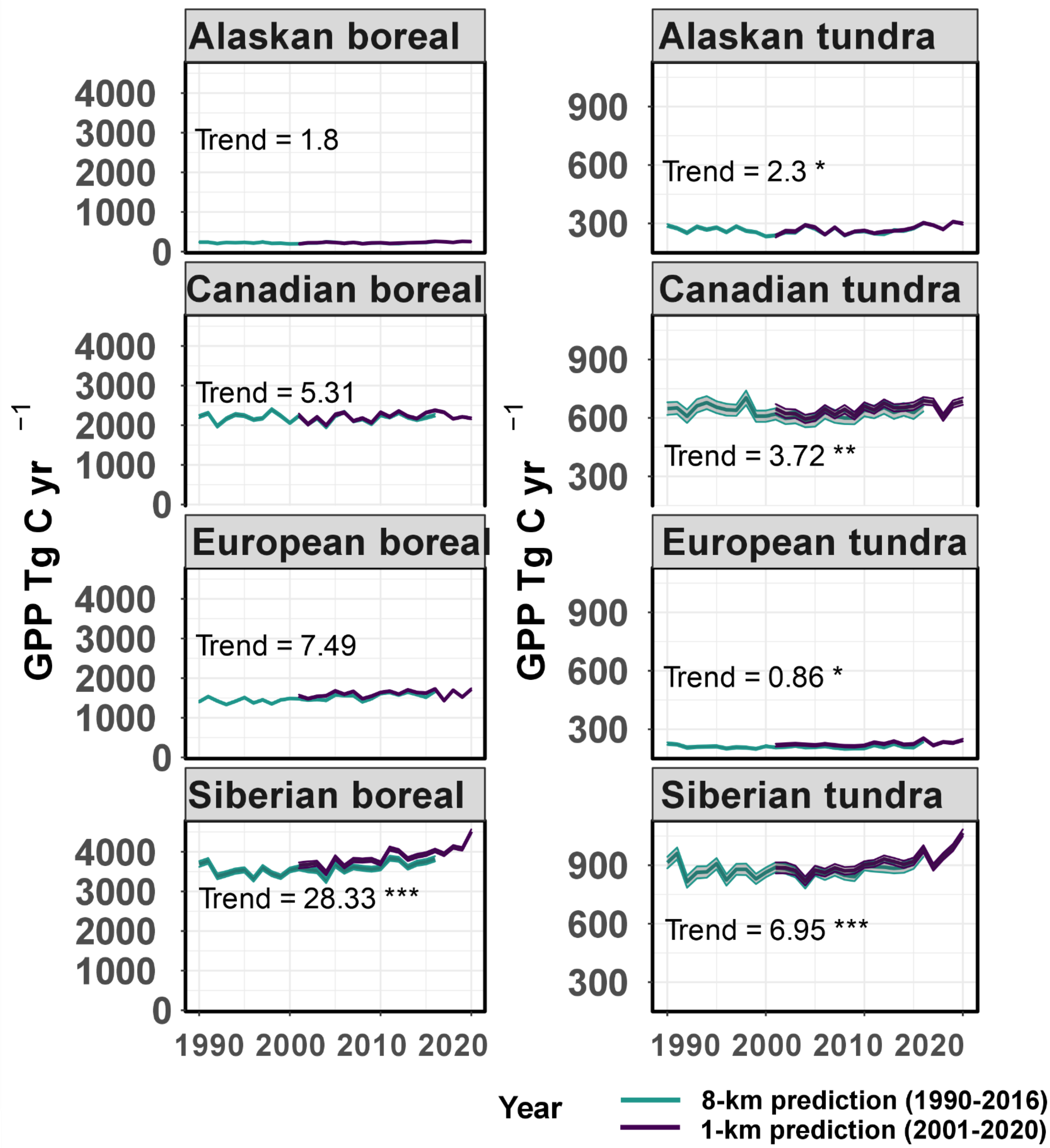

589
590 Supplementary Fig. 21. Time series of GPP across the key regions. Stars in the trend values
591 depict the significance of the trend (*= p<0.05, **=p<0.01, ***=p<0.001).
592
593

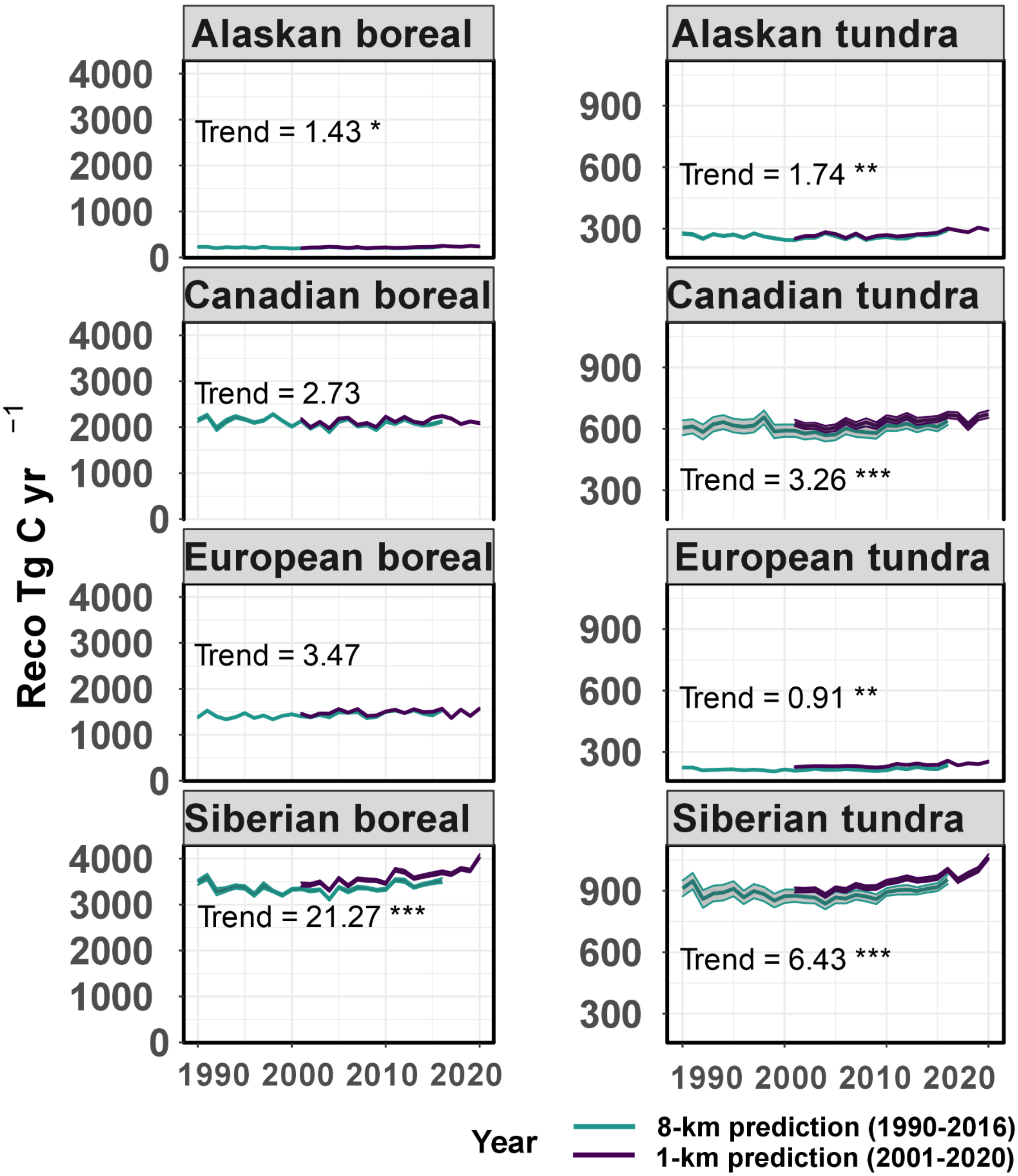

594
595 Supplementary Fig. 22. Time series of R_{eco} across the key regions. Stars in the trend values
596 depict the significance of the trend (*= p<0.05, **=p<0.01, ***=p<0.001).
597
598
599

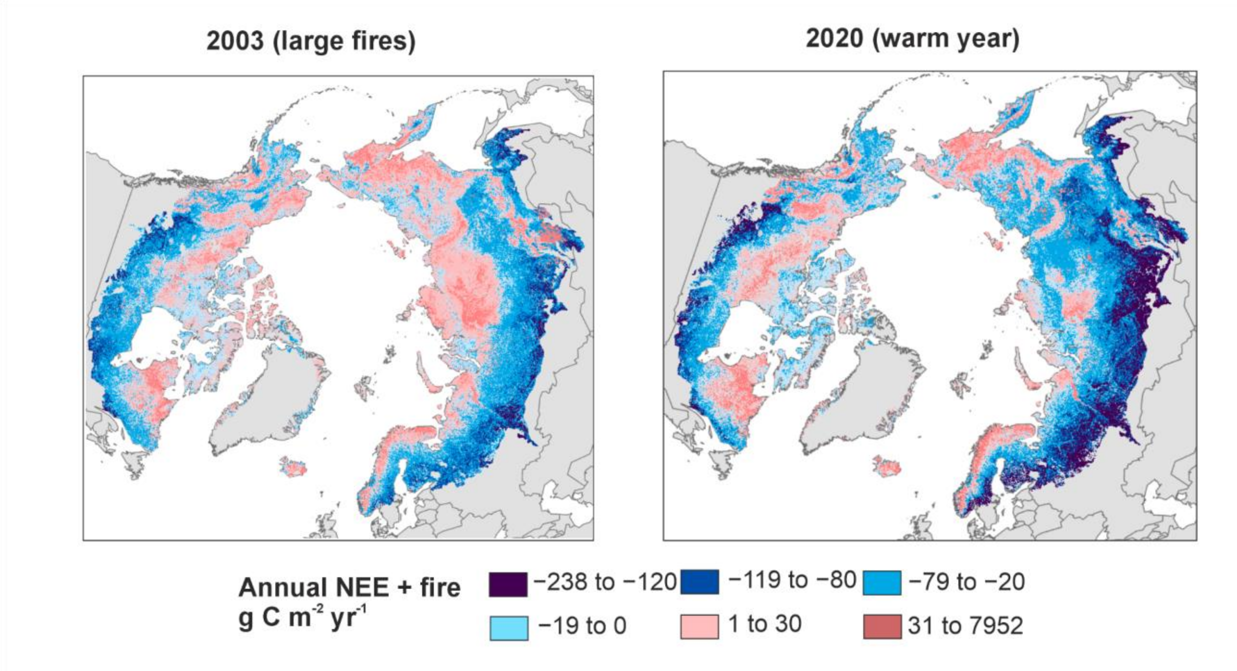

Supplementary Fig. 23. A visualization of how NEE + fire fluxes vary in 2003, when net CO_2 emission budget was the highest, and in 2020, when net CO_2 emission budget was the lowest.

References

1. Dinerstein, E. *et al.* An Ecoregion-Based Approach to Protecting Half the Terrestrial Realm. *Bioscience* vol. 67 534–545 (2017).
2. Obu, J. *et al.* Northern Hemisphere permafrost map based on TTOP modelling for 2000–2016 at 1 km2 scale. *Earth-Sci. Rev.* **193**, 299–316 (2019).
3. Virkkala, A.-M. *et al.* The ABCflux database: Arctic-Boreal CO2 flux observations and ancillary information aggregated to monthly time steps across terrestrial ecosystems. *Earth Syst. Sci. Data* 1–54 (2021) doi:10.5194/essd-2021-233.
4. Virkkala, A.-M. *et al.* The ABCflux Database: Arctic-boreal CO2 flux and site environmental data, 1989-2020. *ORNL DAAC* Preprint at https://doi.org/10.3334/ORNLDAAC/1934 (2021).
5. van Wees, D. *et al.* Global biomass burning fuel consumption and emissions at 500 m spatial resolution based on the Global Fire Emissions Database (GFED). *Geosci. Model Dev.* **15**, 8411–8437 (2022).
6. Pallandt, M. *et al.* Representativeness assessment of the pan-Arctic eddy-covariance site network, and optimized future enhancements. (2021) doi:10.5194/bg-2021-133.
7. Virkkala, A.-M., Virtanen, T., Lehtonen, A., Rinne, J. & Luoto, M. The current state of CO2 flux chamber studies in the Arctic tundra: A review. *Progress in Physical Geography: Earth and Environment* **42**, 162–184 (2018).
8. Euskirchen, E. S. *et al.* Interannual and seasonal patterns of carbon dioxide, water, and energy fluxes from ecotonal and thermokarst-impacted ecosystems on carbon-rich permafrost soils in northeastern Siberia. *J. Geophys. Res. Biogeosci.* **122**, 2651–2668 (2017).

9. Kong, D., Zhang, Y., Gu, X. & Wang, D. A robust method for reconstructing global MODIS EVI time series on the Google Earth Engine. *ISPRS J. Photogramm. Remote Sens.* **155**, 13–24 (2019).
10. Eilers, P. H. C. A perfect smoother. *Anal. Chem.* **75**, 3631–3636 (2003).
11. Du, J., Kimball, J. S. & Watts, J. D. ABoVE: Fractional Open Water Cover for Pan-Arctic and ABoVE-Domain Regions, 2002-2015. (2016) doi:10.3334/ORNLDAAC/1362.
12. Obu, J. *et al.* ESA Permafrost Climate Change Initiative (Permafrost_cci): Permafrost active layer thickness for the Northern Hemisphere, v2.0. (2020).
13. Kim, Y., Kimball, J. S., Glassy, J. & Du, J. An extended global Earth system data record on daily landscape freeze–thaw status determined from satellite passive microwave remote sensing. *Earth Syst. Sci. Data* **9**, 133–147 (2017).
14. Giglio, L., Schroeder, W. & Justice, C. O. The collection 6 MODIS active fire detection algorithm and fire products. *Remote Sens. Environ.* **178**, 31–41 (2016).
15. van der Werf, G. R. *et al.* Global fire emissions estimates during 1997–2016. *Earth Syst. Sci. Data* **9**, 697–720 (2017).
16. Arctic Circumpolar Distribution and Soil Carbon of Thermokarst Landscapes, 2015. https://daac.ornl.gov/SOILS/guides/Thermokarst_Circumpolar_Map.html.
17. Besnard, S. *et al.* Mapping global forest age from forest inventories, biomass and climate data. *Earth Syst. Sci. Data* **13**, 4881–4896 (2021).
18. Breiman, L. Random Forests. *Mach. Learn.* **45**, 5–32 (2001).
19. Takoutsing, B. & Heuvelink, G. B. M. Comparing the prediction performance, uncertainty quantification and extrapolation potential of regression kriging and random forest while accounting for soil measurement errors. *Geoderma* **428**, 116192 (2022).
20. Kuhn, M. Building Predictive Models in R Using the caret Package. *J. Stat. Softw.* **28**, 1–26 (2008).
21. Kuhn, M. The caret package. *R Foundation for Statistical Computing, Vienna, Austria. URL*

https://cran. r-project. org/package= caret (2012).

22. Greenwell, B. M. pdp: An R Package for Constructing Partial Dependence Plots. *R J.* **9**, 421 (2017).
23. Greenwell, B., Brandon, Greenwell, M., Bradley & Boehmke, C. Variable Importance Plots—An Introduction to the vip Package. *The R Journal* vol. 12 343 Preprint at https://doi.org/10.32614/rj-2020-013 (2020).
24. Natali, S. M. *et al.* Large loss of CO2 in winter observed across the northern permafrost region. *Nat. Clim. Chang.* **9**, 852–857 (2019).
25. Emmerton, C. A. *et al.* Net ecosystem exchange of CO2 with rapidly changing high Arctic landscapes. *Glob. Chang. Biol.* **22**, 1185–1200 (2016).
26. Zhang, W. *et al.* Model-data fusion to assess year-round CO2 fluxes for an arctic heath ecosystem in West Greenland (69°N). *Agric. For. Meteorol.* **272-273**, 176–186 (2019).
27. Elith, J., Kearney, M. & Phillips, S. The art of modelling range-shifting species. Methods Ecol Evol 1: 330--342. Preprint at (2010).
28. Jung, M. *et al.* Scaling carbon fluxes from eddy covariance sites to globe: synthesis and evaluation of the FLUXCOM approach. *Biogeosciences* **17**, 1343–1365 (2020).
29. Eyring, V. *et al.* Overview of the Coupled Model Intercomparison Project Phase 6 (CMIP6) experimental design and organization. *Geoscientific Model Development* **9**, 1937–1958 (2016).
30. Talucci, A. C., Loranty, M. M. & Alexander, H. D. Siberian taiga and tundra fire regimes from 2001–2020. *Environ. Res. Lett.* **17**, 025001 (2022).
31. Tramontana, G. *et al.* Predicting carbon dioxide and energy fluxes across global FLUXNET sites with regression algorithms. *Biogeosciences* **13**, 4291–4313 (2016).
32. Jung, M. *et al.* Compensatory water effects link yearly global land CO2 sink changes to temperature. *Nature* **541**, 516–520 (2017).
33. Pastorello, G. *et al.* The FLUXNET2015 dataset and the ONEFlux processing pipeline for

eddy covariance data. *Sci Data* **7**, 225 (2020).

34. Hijmans, R. J. *et al.* Package 'terra'. *Maintainer: Vienna, Austria* (2022).
35. Abatzoglou, J. T., Dobrowski, S. Z., Parks, S. A. & Hegewisch, K. C. TerraClimate, a high-resolution global dataset of monthly climate and climatic water balance from 1958–2015. *Scientific Data* **5**, 1–12 (2018).
36. Lloyd, J. & Taylor, J. A. On the Temperature Dependence of Soil Respiration. *Funct. Ecol.* **8**, 315–323 (1994).
37. Farquhar, G. D. & Sharkey, T. D. Stomatal conductance and photosynthesis. *Annu. Rev. Plant Physiol.* **33**, 317–345 (1982).
38. Grossiord, C. *et al.* Plant responses to rising vapor pressure deficit. *New Phytol.* **226**, 1550–1566 (2020).
39. Durand, M. *et al.* Diffuse solar radiation and canopy photosynthesis in a changing environment. *Agric. For. Meteorol.* **311**, 108684 (2021).
40. Wan et al. (2015). Wan, Z., Hook, S., Hulley, G. (2015). MOD11A2 MODIS/Terra Land Surface Temperature/Emissivity 8-Day L3 Global 1km SIN Grid V006 [Data set]. NASA EOSDIS Land Processes DAAC. Accessed 2021-02-24 from https://doi.org/10.5067/MODIS/MOD11A2.006.
41. Sims, D. A. *et al.* A new model of gross primary productivity for North American ecosystems based solely on the enhanced vegetation index and land surface temperature from MODIS. *Remote Sens. Environ.* **112**, 1633–1646 (2008).
42. Copernicus Climate Data Store. https://cds.climate.copernicus.eu/cdsapp#!/dataset/reanalysis-era5-land?tab=overview.
43. Muñoz-Sabater, J. *et al.* ERA5-Land: a state-of-the-art global reanalysis dataset for land applications. *Earth Syst. Sci. Data* **13**, 4349–4383 (2021).
44. Virkkala, A.-M. *et al.* High-resolution spatial patterns and drivers of terrestrial ecosystem carbon dioxide, methane, and nitrous oxide fluxes in the tundra. *Biogeosciences*

Discussions (2023) doi:10.5194/bg-2023-61.

45. Dorrepaal, E. *et al.* Carbon respiration from subsurface peat accelerated by climate warming in the subarctic. *Nature* **460**, 616–619 (2009).
46. Yi, Y., Kimball, J. S., Rawlins, M. A., Moghaddam, M. & Euskirchen, E. S. The role of snow cover affecting boreal-arctic soil freeze–thaw and carbon dynamics. *Biogeosciences* **12**, 5811–5829 (2015).
47. Arndt, K. A., Hashemi, J., Natali, S. M., Schiferl, L. D. & Virkkala, A.-M. Recent Advances and Challenges in Monitoring and Modeling Non-Growing Season Carbon Dioxide Fluxes from the Arctic Boreal Zone. *Current Climate Change Reports* **9**, 27–40 (2023).
48. K.W. Thoning, A.M. Crotwell, and J.W. Mund. c. 1973-2020. Version 2021-08-09 National Oceanic and Atmospheric Administration (NOAA), Global Monitoring Laboratory (GML), Boulder, Colorado, USA. doi:10.15138/yaf1-bk21.
49. Keenan, T. F. *et al.* A constraint on historic growth in global photosynthesis due to increasing CO2. *Nature* **600**, 253–258 (2021).
50. Raynolds, M. K. *et al.* A raster version of the Circumpolar Arctic Vegetation Map (CAVM). *Remote Sens. Environ.* **232**, 111297 (2019).
51. Sørensen, M. V., Graae, B. J., Classen, A., Enquist, B. J. & Strimbeck, R. Drivers of C cycling in three arctic-alpine plant communities. *Arct. Antarct. Alp. Res.* **51**, 128–147 (2019).
52. LP DAAC - MOD13A1. https://lpdaac.usgs.gov/products/mod13a1v006/.
53. Berner, L. T. *et al.* Summer warming explains widespread but not uniform greening in the Arctic tundra biome. *Nat. Commun.* **11**, 4621 (2020).
54. Box, E. O., Holben, B. N. & Kalb, V. Accuracy of the AVHRR vegetation index as a predictor of biomass, primary productivity and net CO2 flux. *Vegetatio* **80**, 71–89 (1989).
55. Pinzon, J. E. & Tucker, C. J. A Non-Stationary 1981–2012 AVHRR NDVI3g Time Series. *Remote Sensing* **6**, 6929–6960 (2014).

56. DiMiceli, C. *et al.* MOD44B MODIS/Terra Vegetation Continuous Fields Yearly L3 Global 250m SIN Grid V006. (2015) doi:10.5067/MODIS/MOD44B.006.
57. Lafleur, P. M. & Humphreys, E. R. Tundra shrub effects on growing season energy and carbon dioxide exchange. *Environ. Res. Lett.* **13**, 055001 (2018).
58. Hansen, M. & Song, X.-P. Vegetation continuous fields (VCF) yearly global 0.05 deg. (2018) doi:10.5067/MEASURES/VCF/VCF5KYR.001.
59. Hengl, T. *et al.* SoilGrids250m: Global gridded soil information based on machine learning. *PLoS One* **12**, e0169748 (2017).
60. Poggio, L. *et al.* SoilGrids 2.0: producing soil information for the globe with quantified spatial uncertainty. *SOIL* **7**, 217–240 (2021).
61. Walker, D. A. *et al.* Energy and trace-gas fluxes across a soil pH boundary in the Arctic. *Nature* **394**, 469–472 (1998).
62. Virkkala, A.-M. *et al.* Statistical upscaling of ecosystem CO2 fluxes across the terrestrial tundra and boreal domain: regional patterns and uncertainties. *Glob. Chang. Biol.* (2021) doi:10.1111/gcb.15659.
63. Amatulli, G. Geomorpho90m - Global high-resolution geomorphometry layers. (2019) doi:10.1594/PANGAEA.899135.
64. Warner, D. L., Guevara, M., Inamdar, S. & Vargas, R. Upscaling soil-atmosphere CO2 and CH4 fluxes across a topographically complex forested landscape. *Agric. For. Meteorol.* **264**, 80–91 (2019).
65. Obu, J., Westermann, S., Kääb, A. & Bartsch, A. Ground Temperature Map, 2000-2016, Northern Hemisphere Permafrost. (2018) doi:10.1594/PANGAEA.888600.
66. Schuur, E. A. G. *et al.* Permafrost and Climate Change: Carbon Cycle Feedbacks From the Warming Arctic. *Annu. Rev. Environ. Resour.* **47**, 343–371 (2022).
67. Friedlingstein, P. *et al.* Global carbon budget 2022. *Earth Syst. Sci. Data* **14**, 4811–4900 (2022).

68. US Department of Commerce, NOAA & Global Monitoring Laboratory. Global Monitoring Laboratory - Carbon Cycle Greenhouse Gases. (2005).